

Hydrodynamic Groundwater Modeling and Hydrochemical Conceptualization of the Closure Mining Area of the WuMa River Watershed of China

Lei Yang, Lang Liu, Yuan Liu, Guangping Chen, and Liying Liang*



Cite This: *ACS Omega* 2024, 9, 520–537



Read Online

ACCESS |

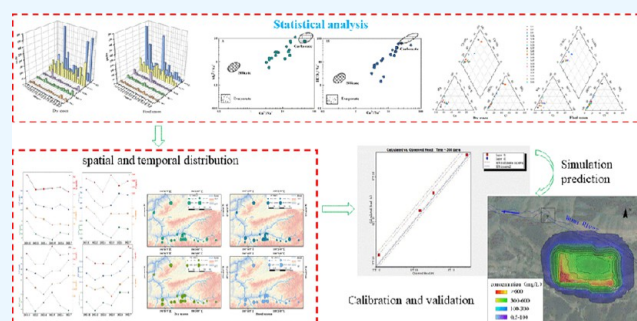
Metrics & More

Article Recommendations

Supporting Information

ABSTRACT: The WuMa River (WMR) watershed is located in Renhuai City, Guizhou Province of China, which is a first-class tributary of the Chishui River. The geochemical investigation mainly included the determination of groundwater pH, total hardness, total dissolution solid, major cationic and anionic, and the geochemical groundwater modeling. The principal component analysis (PCA) and Gibbs model were used to analyze the pollution type and geochemical composition. The geochemical investigation results show that the cations of groundwater are dominated by Ca^{2+} and the anions are dominated by HCO_3^- ; therefore, two main hydrochemical types in the study area are identified as $\text{Ca}^{2+}\text{-Mg}^{2+}\text{-HCO}_3^-$ and $\text{Ca}^{2+}\text{-Mg}^{2+}\text{-SO}_4^{2-}$. The

chemical composition of groundwater in this area is mainly controlled by weathering of the carbonate rocks. The ion concentration of groundwater in the study area exhibited significant spatial variability between dry and wet seasons, while temporal changes of cationic and anionic concentrations exhibited irregularities. In PCA and FA analysis, PC1, PC2, and PC3 were extracted, which could explain 51.92, 26.98, and 12.61% of the total information, respectively. F1 explained 67.44% of the total variance, among which Ca^{2+} , Mg^{2+} , K^+ , SO_4^{2-} , and Cl^- contributed the most among the factors and were the main factors controlling the chemical composition of groundwater. The relative error between the measured water level and the simulated water level is less than 2%, which meets the requirements of simulation accuracy. During the simulation period of the model, a total recharge of $339.05 \times 10^4 \text{ m}^3$ was observed in the simulated area, primarily attributed to infiltration from rainfall. The total excretion amounted to $330.78 \times 10^4 \text{ m}^3$, primarily through evaporation, with a minor amount of lateral outflow. The migration pathway of pollutants in groundwater primarily follows the direction of groundwater flow while diffusing vertically. The migration range of the pollutant is in accordance with the direction of groundwater flow and extends along the larger hydraulic gradient, demonstrating consistency. The findings of this study serve as a reminder that the closure of coal mines can constitute a significant source of water pollution. Simultaneously, they offer empirical data and theoretical references for the simulation and prediction of groundwater contamination in enclosed coal mines.



1. INTRODUCTION

Groundwater is a crucial global resource.^{1,2} In regions and nations where surface water is absent, groundwater serves as the primary source of potable water.^{3–6} According to statistical data, approximately 61% of Chinese cities rely on groundwater as their primary source of drinking water; however, approximately 40% (2.7 Gm³) of China's groundwater has been impacted by mining activities.^{1,7–9} However, the closure of mines has been on the rise year after year due to a variety of factors, including further structural adjustments and resource integration within the coal industry, elimination of excess energy capacity, and safety and environmental protection restrictions.¹⁰ The groundwater environmental issues arising from coal mining have long been a pivotal constraint on local socio-economic and ecological sustainability.^{11–14} However, there are relatively few studies on the heavy metal pollution of groundwater after the closure of

coal mines. Closure of the coal mines, the local groundwater level rises to the water-conducting fissure (or other water-conducting channels) formed during mining, and a hydraulic connection will occur with nearby aquifers, resulting in interlayer pollution.¹⁵ Therefore, the identification of hydro-geochemical processes and hydraulic connections within aquifers in closed coal mines contaminated with pollutants can facilitate an accurate prediction of potential water inrush sources and enable appropriate preventive measures to be taken.

Received: August 15, 2023
Revised: December 5, 2023
Accepted: December 12, 2023
Published: December 27, 2023



The hydrogeochemical evolution of groundwater systems has been extensively explored recently, and air–rock–water interactions are the key mechanisms in most cases.¹⁶ Numerous approaches such as statistical calculations, correlation analysis, Gibbs model, and Piper diagrams are commonly employed for the investigation of hydrogeochemical characteristics, while hydrogeochemical diagrams serve as valuable tools in this regard.^{3,5,13,17} For instance, Zhang et al. conducted a comprehensive investigation of the hydrogeochemical processes and assessed the water quality of mine water in karst collapse columns using hydrochemical, multivariate statistical methods, and stable isotope analyses.¹ The hydrogeochemical components undergo variations along the groundwater flow direction, which is determined by the prevailing hydrogeochemical processes such as mineral dissolution or precipitation, ion exchange, and mixing effects.^{5,17,18} Many hydrogeological studies have been conducted to understand the interactions of groundwater and predict the groundwater in an undamaged groundwater system.^{6,19} A combination of the geometry in the karst aquifer, recharge, and mining exploitation are ignored in current research despite their significance.

In these circumstances, numerical modeling plays a crucial role in facilitating the construction of hydrogeological models and evaluating numerous parameters related to groundwater budgets.^{20–24} The novel technologies of visualization, processing, and modeling have been extensively employed in hydrogeological investigations, such as SWAT, APEX, SEAWAT, FEFLOW, and MODFLOW.^{23–26} MODFLOW is an easily available software package in the public domain. Preziosi et al. conducted a stepwise modeling procedure for groundwater flow simulation by MODFLOW.²⁷ The analysis of these works reveals the challenges associated with obtaining reliable data for a more comprehensive assessment of the intricacies of groundwater systems.

The mining history in most areas has raised significant concerns regarding the availability and suitability of water resources for other sectors. The impacts of mining activities are in terms of both the quality and quantity of water and its flow direction. During mining operations, the water table is artificially lowered through the continuous pumping of water into the mine shafts to maintain dry conditions.²⁸ The recovery of the water table in the mine shafts following mine closure, however, has also had a detrimental effect on water quality. As mine cease and pumping stops, they become filled with highly acidic and mineralized water due to the contact between water and overexposed unmined ore.²⁹ The uncontrolled discharge of contaminated water from abandoned mines, commonly referred to as acid mine drainage (AMD), has resulted in a significant water quality issue.^{30,31} AMD is not only associated with surface and groundwater pollution but is also responsible for the degradation of soil quality and aquatic habitats and for allowing heavy metals to seep into the environment.^{32,33}

The research primarily focuses on active coal mining areas,^{34–36} with less emphasis on the closure ones about groundwater pollution and environmental risk. The research on mine closures has also placed emphasis on groundwater levels,^{37,38} water conservation,^{30,39,40} chemical composition of groundwater,⁴¹ and the air pollution of surrounding. Such as, Kim et al. put forward a simplified model-based program for the analysis and visualization of groundwater rebound in abandoned mines to prevent contamination of water and soils by acid mine drainage.³⁷ Jiang et al. conducted an investigation on the geochemical reaction between karst water in the gob area and

waste gangue with a static immersion experiment to discuss variations in dissolution effects of different types of karst water on gangue after the closure of coal mining.⁴² Zhou et al. found that dual-source iron contributes to the water–solid–gas interaction in abandoned coal mines and the release of iron at different periods after mine closure, posing environmental risks in groundwater and discharging acid mine drainage.¹⁵ Although several studies have examined the impact of coal mine closure, they primarily rely on hydrochemistry and laboratory simulation methods to investigate groundwater flow effects while neglecting the utilization of computer models for simulating and predicting groundwater pollutants.

The Chishui River is a crucial, ecologically sensitive, and fragile area, serving as both a source of drinking water and a national nature reserve for rare and endemic fish in the upper reaches of the Yangtze River. The Wuma River, as a significant tributary of the Chishui River, poses a potential threat to both the environment and society if untreated mine wastewater, contaminated surface water, and groundwater are discharged into the Chishui River subsequent to coal mine closure in the Wuma River Basin. Therefore, it is of great significance to study the risk of water pollution caused by mine closure in the WMR Basin for the protection of the Chishui River. Meanwhile, it is imperative to investigate the scope of groundwater impact and evaluate the prospective pollution level of contaminants.

The closure of coal mines in the WMR watershed, a primary tributary of the Chishui River located in the Renhuai area of Guizhou Province, was considered. The primary concern in this area pertains to the quality of groundwater in relation to closure mining. The controlling processes governing the chemical behavior of groundwater will be investigated from both hydrogeological and hydrogeochemical perspectives. The objectives of this study focus on three aspects:

- (1) investigating the groundwater recharge, runoff, and discharge modes, as well as the aquifer and drinking wellspring with water supply significance, determined the hydrological and geochemical background characteristics of the regional natural karst groundwater system;
- (2) analyzing the pollution forms and pollution ways of the accumulated water in the goaf of the closed coal mine to the regional karst groundwater;
- (3) studying the migration and transformation law of pollutants in the goaf of the closed coal mine in the karst groundwater.

The results provide an accurate prediction of groundwater pollution in the study area's closed pit mine, thereby providing a robust theoretical foundation for effective prevention measures against groundwater contamination.

2. DATA AND METHODS

2.1. Study Area. The WMR is located in Renhuai City, Guizhou Province, which is the first-class tributary of the upper reaches of the Chishui River, China (Figure S1). The geographical location of the study area is between 106°10'–106°27' east longitude and 27°27'–27°47' north latitude.

2.1.1. Physiography. The study area is situated on the eastern bank of the Chishui River and to the south of Renhuai City. The topography in this region comprises undulating mountains, vertical and horizontal valleys, and rugged terrain. The terrain exhibits a concave shape with a low elevation at the center and high elevations on both sides. The highest point, situated in the southernmost Longjing Bay, boasts an elevation of 1299.3 m,

while the lowest point is found at the base of the Chishui River in the north, with an elevation of 435.5 m and a maximum relative difference in elevation reaching 863.8 m. The landform of the area is characterized by mountain plains as well as middle and low mountain canyons. The typical landforms in this area consist of three types: peak clusters with depressions, peak clusters with gullies, and erosion valleys.

2.1.2. Climate and Rainfall. The study area belongs to the subtropical warm and humid monsoon climate area, which has the characteristics of drought in winter and spring, hot and dry in summer, less sunshine in the whole year, rain in early summer and late autumn, and three-dimensional climate and regional differences. The dominant wind direction in the study area is NW throughout the year, and the frequency of quiet wind is high, with an average of 39% and an average wind speed of 1.5 m/s. The annual sunshine is 1266.7 h. The frost-free period is generally 270 to 300 days. The annual average temperature is 18.1 °C, the maximum annual average temperature is 22.1 °C, the extreme maximum temperature is 43 °C, the minimum annual average temperature is 15.1 °C, and the extreme minimum temperature is 1.9 °C below zero. The annual average rainfall is 1235.6 mm, the annual maximum rainfall is 1339.6 mm (2014), and the minimum rainfall is 881.7 mm (2013).

2.1.3. Drainage. In the western part of the study area, Longjing, Jiucang, Yuanjiazhai, Firestone, Tianbazhai, Madong, and other places take the Jiucang River as the drainage boundary. The whole central and eastern regions are drained by the WMR. The WMR flows from east to west in the study area, turns from Wuma Town, and flows from south to north to the Chishui River. It is fed at the border on both sides and dispersed into the WMR through surface gullies or underground rivers. The main recharge areas of the underground karst are Changgang town in the east and Sanyandong in the middle.

2.1.4. Hydrogeology. According to the lithology, water-bearing medium type, and groundwater occurrence conditions, there are three types of groundwater in the study area: carbonate karst water, bedrock fissure water, and loose rock pore water.

(1) Carbonate Karst Water. According to the occurrence medium and hydrodynamic characteristics of karst water, it can be divided into two subcategories: karst cave pipe water dominated by limestone and cave fissure water dominated by dolomite.

(1.1) Limestone Cave Pipe Water. The major aquifer lithostratigraphic units comprise the Shizishan Formation (T2sh), Jialingjiang Formation (T1-2j), second Member of Yelang Formation (T1y2), Changxing Formation (P3c), Qixia Maokou Formation (P2q + m), and Qingxudong Formation (E1q).

The lithology consists of limestone and dolomitic limestone, with a highly karstified aquifer system characterized by well-developed surface karst features such as depressions, water caves, underground river skylights, and karst hard wells that occur in a linear pattern along the structural trend.

This subclass of karst water exhibits characteristics such as concentrated runoff, high discharge rates, rapid flow velocities, significant dynamic fluctuations, and strong cyclic alternations. The water-rich grade index of the water-bearing rock group indicates that this type exhibits a moderate to strong degree of water richness, although its water content is highly heterogeneous.

(1.2) Dolomitic Fissure Water. The main water-bearing rock groups include the Gaotai Formation (E2g), Loushanguan Group (E0l), and Tongzi Honghuayuan Formation (O1t-h).

The lithology is thick-bedded dolomite, argillaceous dolomite, and calcareous dolomite. In the geomorphology, it is mostly formed in mild valleys and gullies, and the replenishment conditions are good. The karst water in dolomite karst pores and dissolved gaps has the characteristics of dispersed runoff, slow velocity, uniform water richness, and little dynamic change. According to the water-rich grade index of the water-rich rock group, the water-rich rock group is medium to strong.

(2) Bedrock Fissure Water. It is mainly distributed in the Jurassic (J), Upper Triassic Shaxujiahe Formation (T3xj), the third member of Yelang Formation (T1y3) argillaceous siltstone, silty mudstone, carbonaceous mudstone, mudstone, local sandstone, limestone, and coal seam areas and is weathering fissure and structural fissure water, with an obvious topside supporting effect and many characteristics of topside water retention. Aquifer water richness is weak—medium.

(3) Pore Water of the Unconsolidated Layer. It is scattered in karst depressions, valleys, and river valleys, and the water-bearing medium is the pores in the quaternary alluvial, residual slope deposit clay, subclay, subsandy soil, and sand gravel layers, containing pore water. The performance is relatively scattered, seasonal, has no water in drought and has poor water richness.

2.1.5. Aquifer. The strata in the study area exhibit a generally monoclinical structure, with a dip angle ranging from approximately 6 to 15° and an inclination angle of 30 to 38°. However, faults and folds are not prominently developed within this region. According to the lithology combination, water-containing and water-retaining layers, the main aquifers are the middle Yelang Formation limestone (T1y2), Changxing Formation limestone (P3c), and Maokou Formation (P2m). Due to the influence of mining, the Upper Permian Longtan Formation (P3l) formed goaf and a large number of crushing areas. The water-isolated layer is the lower and upper member mudstone (T1y1, T1y3) of the Yelang Formation and the nongoaf area of the Permian Longtan Formation (P3l), as shown in Figure S2.

2.2. Methodology. **2.2.1. Model Conceptualization and Data Acquisition.** The MODFLOW model is a physically based, distributed finite difference that operates in three dimensions and simulates variably saturated subsurface systems, which has been used and tested in various practical cases.^{43,44} Available processes to be simulated in MODFLOW include groundwater recharge, vadose zone percolation evapotranspiration, pumping, and discharge to subsurface drains and river–aquifer interactions.^{45–47} In addition, the model can effectively simulate the movement of groundwater flow, ions, and pollutants within the study area while also validating the simulation results and adjusting parameters based on measured data of relevant substances in the research site.^{48,49} The Modflow model is contingent on the resolution of the diffusivity equation, represented by the following equation⁴⁸

$$\frac{\partial}{\partial x} \left(K \frac{\partial H}{\partial x} \right) + \frac{\partial}{\partial y} \left(K \frac{\partial H}{\partial y} \right) + \frac{\partial}{\partial z} \left(K \frac{\partial H}{\partial z} \right) + W = S_y \frac{\partial H}{\partial t} \quad (x, y, z) \in \Omega, t > 0 \quad (1)$$

$$H(x, y, z, t)|_{t=0} = H_0(x, y, z) \quad (x, y, z) \in \Omega \quad (2)$$

$$H(x, y, z, t)|_{S_1} H_1(x, y, z, t) \quad (x, y, z) \in S_1 \quad (3)$$

$$K \frac{\partial H}{\partial t} \Big|_{S_2} = q(x, y, z, t) \quad (4)$$

where H is the aquifer level, H_0 is the initial aquifer level, K is the permeability coefficient, S_y is the water yield of the aquifer (dimensionless), W is the sink term, S_1 and S_2 are head boundary and flow boundary, respectively, q is the second type of single-width flow on the boundary, and t is the time.

The selection of WMR as the research area was primarily based on two key factors: first, the presence of a significant number of decommissioned coal mines dispersed throughout both sides of the basin; second, the topography of the Wuma karst landform characteristics and rock layers. According to the coal resource distribution in Renhuai City, there are a total of 41 pairs, with all 27 pairs in the upper reaches of the Maotai coal mine situated within the Wuma River basin; notably, these mines are categorized as small-scale operations.

2.2.2. Model Identification and Validation. The identification and verification of the model constitute a continuous process of iteratively inverting and testing the numerical model, which is also an indispensable component for successfully establishing the numerical model. The model achieves a high level of reliability and demonstrates excellent agreement with the actual groundwater system through the continuous refinement of hydrogeological parameters. The model calibration should be conducted based on the following principles: for instance, the dynamic groundwater process and the simulated and actual groundwater systems' flow field ought to exhibit fundamental consistency, specifically in terms of resembling the contour of the groundwater level. The simulated hydrogeological parameters and changes in groundwater balance should be essentially congruent with the actual conditions. The identification and verification of the model constitute a continuous process of iteratively inverting and testing the numerical model, which is pivotal for successfully establishing the numerical model. The model achieves a high level of reliability and demonstrates excellent agreement with the actual groundwater system through continuous refinement of hydrogeological parameters.

In order to ensure the model's compliance with the structural and functional characteristics of the groundwater system, as well as its accurate and reliable depiction of dynamic changes in the system, January 2019–January 2020 has been chosen as the identification and validation period for this simulation. This selection aligns with the requirement of encompassing one hydrological year. The duration of one stress period is defined as one month, and within each stress period, there are three calculation time steps. During the model identification and verification stage, the 2019–2020 borehole water level observation data from the mining area are utilized to assess the goodness of fit between simulated and actual groundwater levels, building upon previous data collection and investigation findings. The month of January 2020 is designated as the validation period for model identification.

2.2.3. Groundwater Extraction by Pumping. The permeability coefficients of aquifers in the quaternary system and Jialingjiang Formation range from 8.62×10^{-5} to 5.23×10^{-4} cm s^{-1} . The permeability coefficient of limestone solution fissure aquifer ranges from 8.27×10^{-5} to 1.23×10^{-4} cm s^{-1} . The permeability coefficient of the ash solution fissure aquifer in the Maokou Formation from previous work ranges from 3.74×10^{-4} to 6.37×10^{-4} cm s^{-1} . In the process of model establishment, the

final parameter values of each partition are determined according to the initial parameter values obtained (Table S1), and then, the final parameter values of each partition are determined through the fitting and calibration of the model.

2.2.4. Boundary Conditions. According to the water level geological map of Guizhou Province (Figure S3), the WMR is divided from east to west in the study area (the red box in the figure below is the study area, the blue line is the WMR), Longtan Formation, Changxing Formation, Yelang Formation, and Jialingjiang Formation. The Chaiyuan Coal Mine is located in Chaiyuan Village, Changgang Town, south of Renhuai City, Guizhou Province, north of Luban Town, west of Wuma Town, 50 km away from Renhuai City. The mine is about 1.8 km long from east to west and 0.8 km wide from north to south, with a flat mine area of 1.44 km^2 . Its geographical coordinates are $106^\circ 23' 54''$ – $106^\circ 25' 12''$ east longitude and $27^\circ 37' 07''$ – $27^\circ 37' 59''$ north latitude. The nearest horizontal distance from the river on the northeast side of the closure area is about 150 m, and the vertical distance is about 350 m.

Visual MODFLOW software was used to establish a 7000 m \times 5800 m numerical simulation area. The simulation area was divided into 100 m \times 100 m grids on planes X and Y and the mining area was encrypted near the mining area and divided into 50 m \times 50 m grids for accurate calculation in the later stage. At the same time, according to the division of boundary conditions in the study area, the grid outside the simulation range was set as inactive cells, that is, this part of the grid does not participate in the calculation of the model, and its effective simulation area is 21.3 km^2 . The model grid is divided as shown in Figure S4.

The initial step in calibrating the model involved running it without any modifications to identify areas of discrepancy. For the subsequent step, namely, the calibration in steady state conditions, the permeability values of each aquifer level were modified through a trial-and-error approach while considering the initial values obtained from the pumping test presented in the conceptual model section. After conducting numerous manual calibration tests, the observed and simulated water heads exhibited a high degree of similarity.

2.3. Geochemical Analysis and Multivariate Statistical Approaches.

2.3.1. Sample Collection. Prior to sample collection, the water sample is filtered on-site using a 0.45 μm nylon filter. When collecting, the filtered water sample is packed into two different volumes (30 and 250 mL). Polyethylene bottles with different internal environments were tested for different indicators, among which 250 mL polyethylene bottles were cleaned with 6 mol/L nitric acid in advance, and their internal environment was adjusted to $\text{pH} < 2$ for cationic test analysis. The 30 mL polyethylene bottle is washed in pure water and not acidified for anion analysis. In the process of pouring, the bottle needs to be filled to achieve the purpose of draining the air in the bottle. After collection, wrap a sealing film around the mouth of the bottle and store the sample bottle at 4 $^\circ\text{C}$ until the sample is tested.

The spatial samples were collected in different months in different seasons. In August 2020, September 2021, December 2021, and February, April, May, June, July, and August 2022, a total of 34 samples were collected each time, including 5 mine water, 9 surface water, 19 wellspring water, and 1 karst cave water (Figure S1).

All samples in the study area were tested at the State Key Laboratory of Loess and Quaternary Geology (SKLLQG), Institute of Earth Environment, Chinese Academy of Sciences. The detection indexes include macroions (K^+ , Na^+ , Ca^{2+} , Mg^{2+} ,

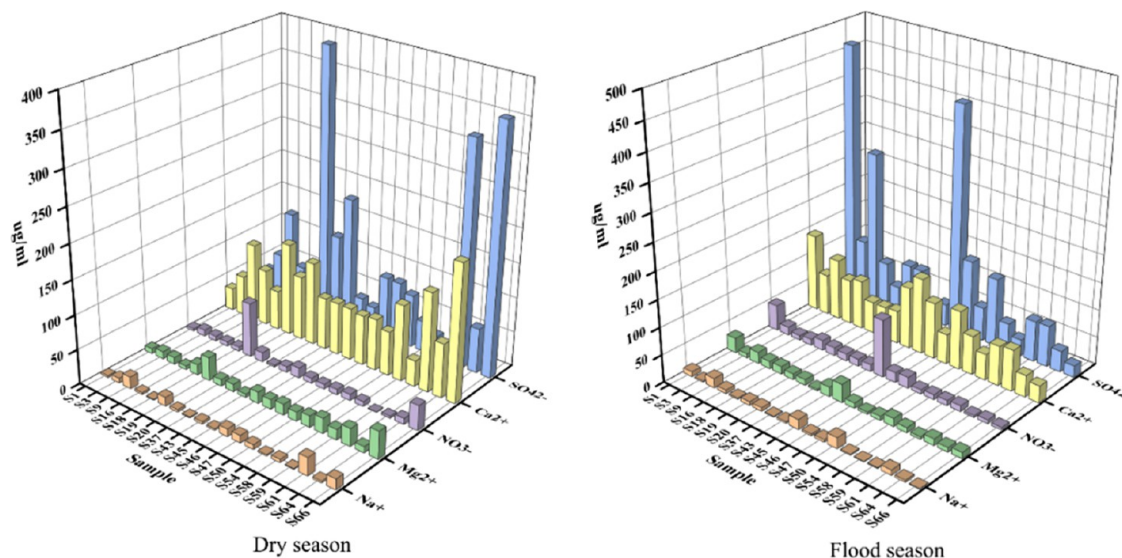


Figure 1. Analysis of major anion concentration distribution in groundwater.

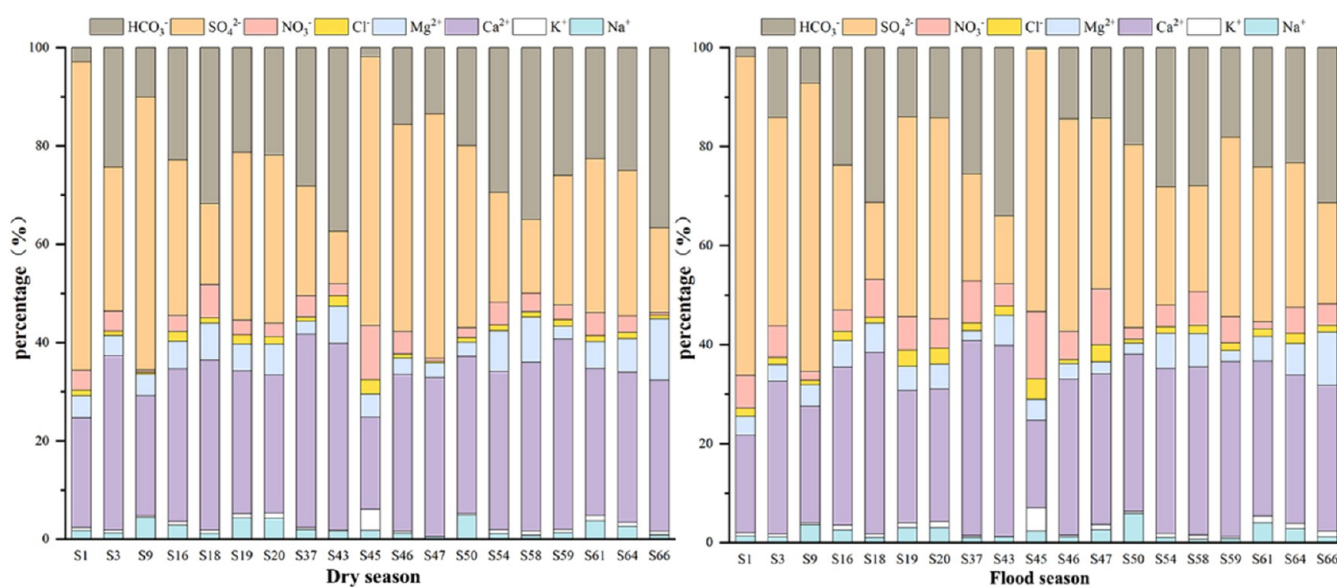


Figure 2. Percentage of ionic and anion concentrations in groundwater.

Cl^- , SO_4^{2-} , NO_3^- , F^-). General trace elements (Li, Be, B, Mn, Fe, Co, Al, Cu, Zn, As, Se, Rb, Y, Cd, Ba, Ti, U). The cations were determined by inductively coupled plasma optical emission spectroscopy (ICP-OES), and the anions were determined by a Dionex-600 ion chromatograph. The test accuracy of the macroion index is 0.01 mg/L, and the test error is less than 2%. Trace element testing uses inductively coupled plasma mass spectrometry (ICP-MS). The standard sample is N9300723, and the relative standard deviation (RSD) value should be less than 1% during the test. The concentration of HCO_3^- in water samples within the study area was calculated by charge conservation. In order to test the reliability of the data, 10 samples were randomly selected to titrate the concentration of dissolved inorganic carbon (DIC) in the water samples by the Meck alkalinity test, with an accuracy of 0.05 mM. Finally, the relative deviation rate between DIC concentration and HCO_3^- concentration was calculated. The results show that if the relative deviation rate is less than 5%, the HCO_3^- concentration calculated by charge conservation is considered to be reliable.

2.3.2. Data Processing. Principal component analysis and factorial analysis are multivariate statistical techniques commonly performed to reduce the size of large data sets. These methods are operated to explore variable proportionality and are frequently employed in environmental studies with a high degree of temporal or spatial variation.

The data processing and image rendering software involved in this study are shown in Table S2.

3. RESULTS AND DISCUSSION

3.1. Hydrochemistry of Groundwater. The pH values of the WMR watershed groundwater are 5.03 to 8.27. The pH value of the groundwater varies from 5.03 to 8.61, indicating that the water samples are weakly acidic to weakly alkaline in nature, and the average pH value of the dry, normal, and wet periods is 7.69, 7.64, and 7.31, respectively. The results indicate that dissolved carbonates in water samples mainly existed in the form of HCO_3^- . The electrical conductivity (EC) value of groundwater varies from 173 to 1221, with average values of 572.11,

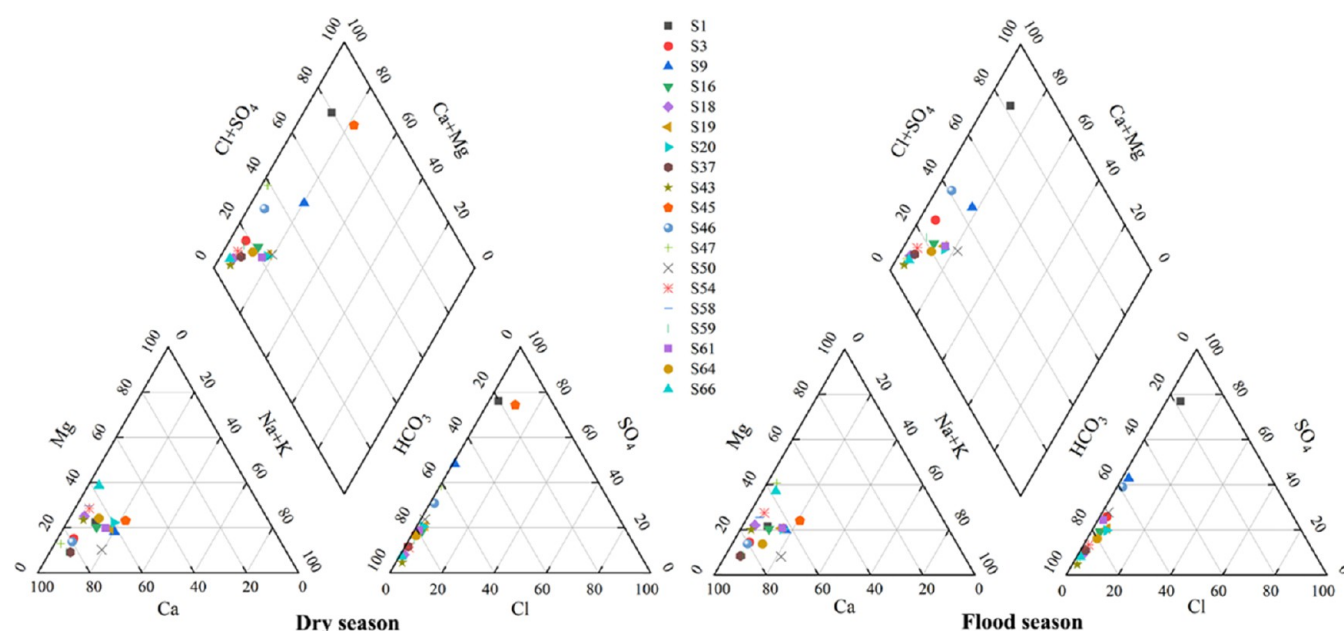


Figure 3. Piper chart of the chemical composition of groundwater.

519.4, and 536.3 $\mu\text{S}/\text{cm}$ in the dry season, normal season, and wet season, respectively. The large variation range and standard deviation indicate that the pH and EC of each water sample are different in space, and the hydrochemical composition of the study area is not uniform. This may be attributed to diverse lithologies, geochemical processes, and hydrological conditions within the mining region. The major cationic and anionic concentrations and percentages in 19 groundwater samples were illustrated during dry and wet periods in Figures 1 and 2. The major cationic concentrations follow the order of $\text{Ca}^{2+} > \text{Mg}^{2+} > \text{Na}^+ > \text{K}^+$, with Ca^{2+} being the predominant one, ranging from 29.52 to 249 mg/L. The average concentrations of Ca^{2+} during dry, normal, and wet periods were 87.36, 76.92, and 88.01 mg/L, respectively. Second, Mg^{2+} is the ion with a higher concentration, ranging from 3.92 to 45.6 mg/L. The mean values of Mg^{2+} during the dry season, normal season, and wet season are 15.83, 14.03, and 14.76 mg/L, respectively. The anion concentration in groundwater follows the order of decreasing magnitude: $\text{SO}_4^{2-} > \text{HCO}_3^- > \text{NO}_3^- > \text{Cl}^-$. HCO_3^- and SO_4^{2-} are the primary anions, with a variation range of 20.93–558.35 mg/L for SO_4^{2-} and average values of 119.2, 112.9, and 113 mg/L during dry, normal, and wet periods, respectively. The concentration of HCO_3^- ranged from 13.29 to 108.26 mg/L, with mean values of 52.78, 46.13, and 44.47 mg/L during the dry, normal, and wet seasons, respectively.

Analytical results of groundwater analysis were plotted on a trilinear diagram (Piper) (Figure 3). The Piper diagram depicts the relative concentrations of various ions in each water sample to demonstrate trends in different geochemical characteristics and types of groundwater composition that are prevalent within the study area. The Piper diagram reveals that the groundwater composition types remain consistent between dry and wet periods, with no significant variation in ion concentration distribution across different sampling times or locations. The majority of the samples exhibit a preponderance of Ca^{2+} cations and HCO_3^- anions. In addition, the predominant anion found in groundwater samples collected from sampling points S1 and S3 is sulfate (SO_4^{2-}). Based on the concentration of the major ions, two predominant hydrochemical types were identified in the

study areas $\text{Ca}^{2+}-\text{Mg}^{2+}-\text{HCO}_3^-$ and $\text{Ca}^{2+}-\text{Mg}^{2+}-\text{SO}_4^{2-}$. Similar hydrochemical types also were found in a closed coal mine in Zibo City, Shandong Province.¹⁵ Large quantities of Ca^{2+} , Mg^{2+} , HCO_3^- , and SO_4^{2-} in groundwater indicate that calcite and gypsum are abundant during weathering. Higher calcium concentrations in groundwater may result from the weathering of minerals that form calcareous rocks, which release more calcium ions into the groundwater.

The concentration range of some trace elements in groundwater in the study area is as follows: Li ranges from 0.19 to 38.7 $\mu\text{g}/\text{L}$, B ranges from 3.17 to 71.2 $\mu\text{g}/\text{L}$, Al ranges from 0.6 to 2609.6 $\mu\text{g}/\text{L}$, Mn ranges from 0 to 2415.4 $\mu\text{g}/\text{L}$, Cu ranges from 0 to 8.17 $\mu\text{g}/\text{L}$, Zn ranges from 0 to 500.1 $\mu\text{g}/\text{L}$, As ranges from 0 to 1.62 $\mu\text{g}/\text{L}$, Se ranges from 0 to 9.17 $\mu\text{g}/\text{L}$, and Rb ranges from 0.02 to 28.98 $\mu\text{g}/\text{L}$. The order of trace element concentration from high to low is $\text{Mn} > \text{Al} > \text{Zn} > \text{B} > \text{Li} > \text{Rb} > \text{Se} > \text{Cu} > \text{As}$. The concentration of trace elements in the dry season was significantly higher than that in the wet season. The concentration of Mn exceeded the drinking water standard for groundwater in China. The excessive concentration of Mn in drinking water will cause health hazards to the human body.^{50,51} However, the concentrations of Fe in groundwater are almost always below the detection limits. It can be observed from Figure S5 that the concentration of other trace elements in groundwater is generally low and does not exceed the ideal limit for drinking water. It can be observed from Figure S5 that the concentration of trace elements in groundwater is generally low and does not exceed the ideal limit for drinking water.

3.1.1. Statistical Analysis and Groundwater Mineralization Processes. The statistical analysis was established for 8 variables (K^+ , Ca^{2+} , Na^+ , Mg^{2+} , Cl^- , NO_3^- , SO_4^{2-} , and HCO_3^-) and 180 individuals (groundwater samples). The correlation matrix between the study parameters is presented in Tables S3 and S4. Ionic ratios have proven to be invaluable in providing profound insights into the intricate chemical processes and phenomena that govern the chemistry of water. The correlation coefficients between cations and anions underwent changes during both the wet and dry seasons, with particular emphasis on the interplay between SO_4^{2-} and Ca^{2+} . Ca^{2+} was positively correlated with

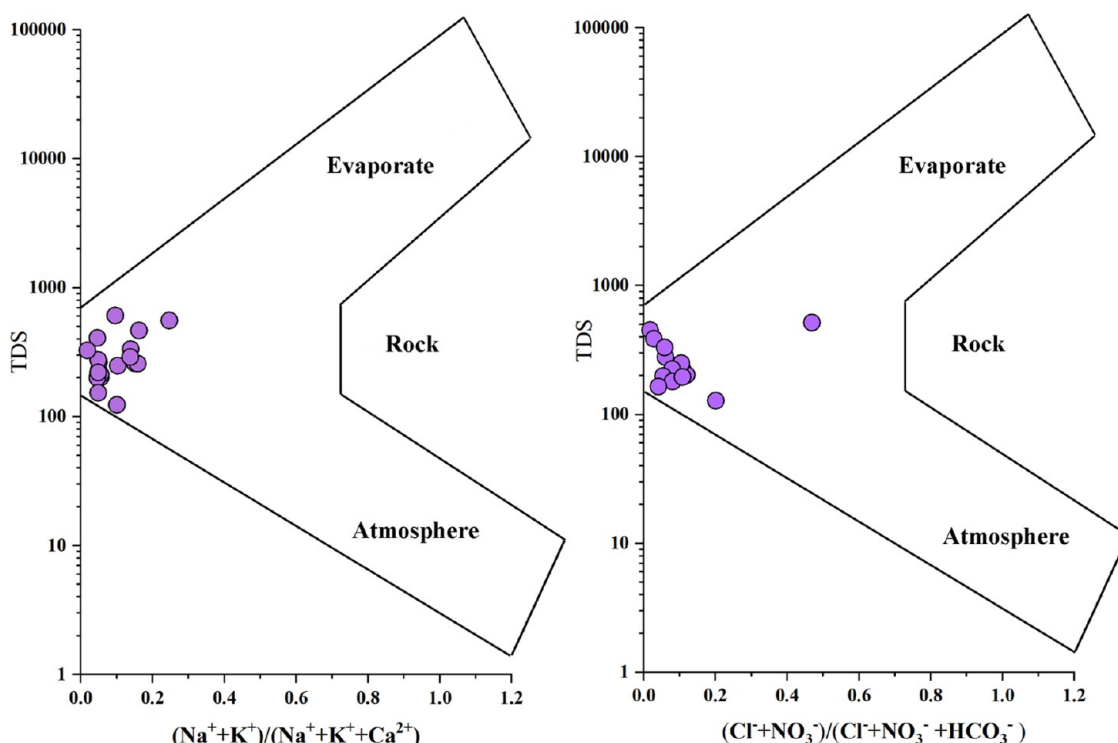


Figure 4. Gibbs map of groundwater samples.

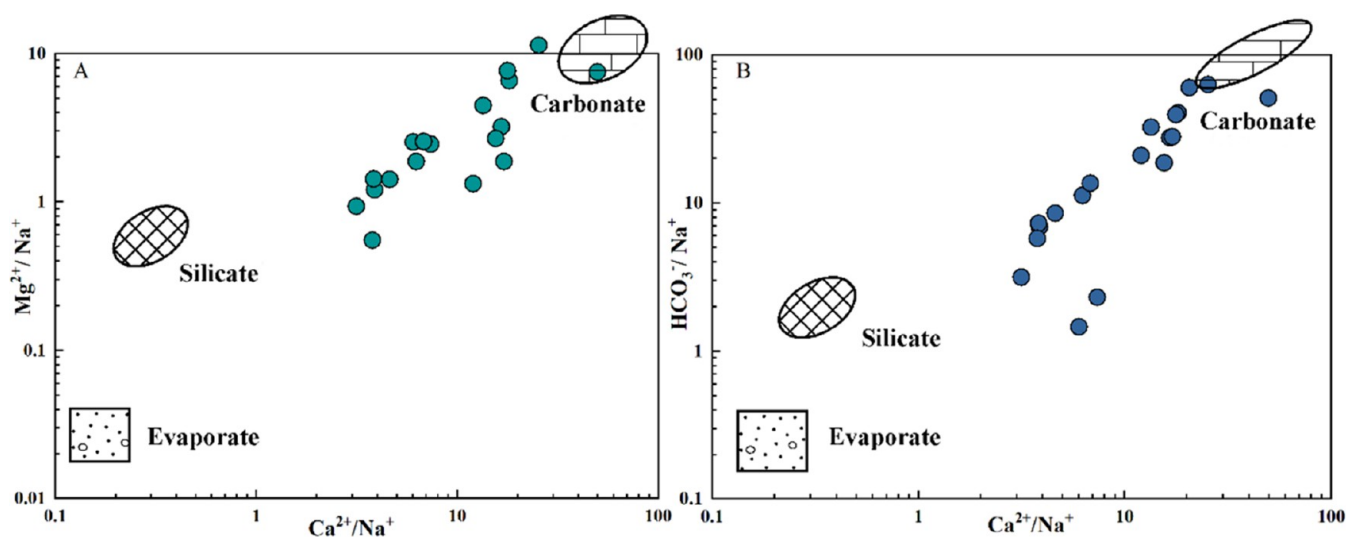


Figure 5. $\text{Ca}^{2+}/\text{Na}^{+}$ vs. $\text{Mg}^{2+}/\text{Na}^{+}$ and $\text{Ca}^{2+}/\text{Na}^{+}$ vs. $\text{HCO}_3^{-}/\text{Na}^{+}$ in groundwater.

Mg^{2+} and SO_4^{2-} , and the correlation coefficients were 0.727 and 0.897, respectively, indicating that they had a common origin, and that was basically consistent with the early research.⁵² The correlation coefficients between NO_3^{-} , K^{+} , and Cl^{-} were as high as 0.926 and 0.905, indicating that the chemical composition of groundwater in the study area may be disturbed by human activities. Nevertheless, there was no significant correlation between Na^{+} and Cl^{-} during the dry season; however, a strong correlation was observed during the wet season. The source of Na^{+} ions could be the dissolution of the clayey sand layers, which are quite common and easy to dissolve. Between water and clayey sand minerals, there is usually an adsorption of Ca^{2+} and release of Na^{+} .⁵³

The Gibbs model can qualitatively determine the sources of groundwater chemical composition, including evaporation and concentration, rock weathering, and atmospheric input. Figure 4 illustrates that the distribution of groundwater samples in the study area is primarily concentrated in regions where rock weathering dominates, indicating that rock weathering plays a significant role in shaping the chemical composition of groundwater within the study area. Using the ratio relationship among $\text{Ca}^{2+}/\text{Na}^{+}$, $\text{Mg}^{2+}/\text{Na}^{+}$, and $\text{HCO}_3^{-}/\text{Na}^{+}$ in groundwater, the Na end-element map can be utilized to assess the impact of different lithologies on the chemical composition of groundwater in this area, including silicate rock, carbonate rock, and evaporative rock (Figure 5). However, it is closer to the end member of carbonate rock, indicating that the chemical

composition of groundwater in this area is mainly controlled by the weathering of carbonate rock, and some points fall in the middle of silicate rock and carbonate rock, indicating that silicate rock also has a certain influence on the hydrochemical composition of this area. Similar kinds of phenomena have also been reported.^{54,55} The rock weathering types of different sampling sites are different, which may be related to the spatial lithology differences in the study area.

3.1.2. Principal Component Analysis (PCA) and Factorial Analysis (FA). Factor analysis is a crucial statistical technique for elucidating the hydrochemistry of groundwater.^{56,57} The method employs a multivariate statistical approach to establish a general relationship among the measured chemical variables, revealing multivariate patterns that facilitate the classification of the raw data. The geochemical composition of groundwater is influenced by two primary factors: weathering processes and anthropogenic inputs. Principal component analysis (PCA) utilizes Varimax rotation and Kaiser normalization to reduce variables and dimensions, thereby elucidating the relationship between cluster variables and calculating the contribution of each factor to the chemical composition of groundwater.⁵⁸ In this study, three principal components, PC1, PC2, and PC3, were extracted, which could explain 51.92, 26.98, and 12.61% of the total information, respectively (Table S5). PC1 is the most influential factor, and the main indicators associated with this factor were F^- , SO_4^{2-} , Fe, Mn, Cu, Zn, and pH. Among them, pH exhibited a strong negative correlation (-0.866) with the factor, while other indicators such as SO_4^{2-} , Mn, Cu, and Zn demonstrated significant positive correlations of 0.604, 0.948, 0.859, and 0.964, respectively. Given that the water samples were collected exclusively from mines within the Wuma River Basin, it can be inferred that a large number of sulphur-containing coal seams and deposits (CuS, ZnS) were exposed to the environment during mining operations, which continued until the cessation of mining activities. Therefore, with the assistance of air, water, and microorganisms, a series of physical and chemical reactions including dissolution, hydrolysis, and oxidation take place to generate acidic wastewater containing a significant concentration of heavy metal elements (Mn, Cu, Zn) and exhibiting a low pH level (2–4). The above analysis suggests that the PC1 factor may potentially indicate the input of acid mine wastewater. Paciuszkiewicz et al. demonstrated that the closure and flooding triggered acid mine drainage that has resulted in mildly acidic pH and higher concentrations of several metals with the concentration of nickel (418 $\mu\text{g/L}$), zinc (1161 $\mu\text{g/L}$), and manganese (11,909 $\mu\text{g/L}$).⁵⁹ The variables closely associated with the PC2 factor are Na^+ , SO_4^{2-} , and total hardness, with coefficients of 0.608, 0.702, and 0.859, respectively. The strong correlation between them is consistent with the chemical characteristics of groundwater. Based on the Piper diagram above, it has been found that the predominant chemical composition of the Wuma River Basin primarily consists of Ca^{2+} – Mg^{2+} – HCO_3^- , followed by Ca^{2+} – Mg^{2+} – SO_4^{2-} . Under the long-term dissolution of groundwater and the surrounding parent rock, the hardness and salinity increase continuously. Based on the above analysis, it is speculated that the PC2 factor may represent the input of underground rock weathering. The closely related variable in the PC3 factor is Na, and the load coefficient is 0.754. According to the 2020 land use monitoring data, the predominant land use types in the Wuma River Basin comprise cultivated land (39.2%) and forest land (38.5%), while anthropogenic activities potentially influence the hydrochemical composition of mine water. Furthermore,

occasional human activities within the enclosed mining area will also exert a discernible influence on the composition of mine water. Hence, it is plausible that PC3 may originate from an anthropogenic source.

Two principal components (F1 and F2) were extracted with eigenvalues greater than 1, indicating their significant contribution to the overall variance of the data (Table S6). The F1 factor explains 67.44% of the total variance, with Ca^{2+} , Mg^{2+} , K^+ , SO_4^{2-} , and Cl^- being the major contributors. Contributing the most among the factors, factor 1 represents the natural hydrogeochemical evolution resulting from the groundwater–rock interaction. The result of F1 is consistent with the result of PCA, which is derived from the hydrochemistry of the earth. This phenomenon can be attributed to chemical weathering, which leads to the dissolution of rocks and minerals in sediments. The process of groundwater–rock interaction is characterized by the enrichment of groundwater through the presence of sulfate, calcium, potassium, chloride, and magnesium.¹ This study is similar to other studies.^{60,61} And the statement suggests that karst processes exert a dominant influence on groundwater in this region. F2 displays a relatively high concentration of Na^+ and HCO_3^- , accounting for 18.72% of the total variance, indicating that the halite dissolves in groundwater enrichment by sodium and carbonate.^{18,54} The F2 result is in accordance with that of PCA2 and is obtained from rock weathering.

Based on the temporal and spatial distribution of groundwater chemical composition, a spatial interpolation diagram was generated for the concentrations of SO_4^{2-} in groundwater (Figure S6). The results indicate that the water samples from S1, S9, and S45 are not contaminated with sulfate except for exceeding the class III water quality standard in terms of sulfate content. The chemical properties of groundwater in mining areas are subject to variations depending on the geographical location and hydrological conditions. Under acidic conditions, the dissolution of pyrite in coal-measuring formations with a specific composition can result in sulfide dissolving into groundwater and causing high levels of sulfate pollution. However, the absence of Fe in groundwater within the study area suggests that the impact of pyrite oxidation on sulfate may be limited.³ The presence of Mg^{2+} and Ca^{2+} in groundwater exhibits a significant correlation with SO_4^{2-} (as shown in Tables S3, S4). Both the Gibbs diagram and Na end-element diagram indicate that rock weathering and dissolution dominate the chemical composition of groundwater.^{1,62,63} Therefore, the high sulfate content observed in this study area may be attributed to a substantial amount of calcareous shale or limestone components present within the coal-bearing strata.

3.1.3. Spatial Variations of Main Ions. (1) Spatial Distribution Characteristics of Main Ions. The spatial distribution of Ca^{2+} and Mg^{2+} in groundwater during dry and wet seasons in the study area is illustrated in Figure S7. The ion concentrations varied significantly across various sampling points. The highest concentrations of Ca^{2+} and Mg^{2+} were observed at S1 and S9, followed by those at S43, S45, S47, and S50. Groundwater Ca^{2+} and Mg^{2+} may originate from the dissolution of carbonate rocks (e.g., calcite and dolomite) as well as the oxidation of sulfide-rich coal seams and deposits. Figure S8 illustrates the spatial distribution of SO_4^{2-} and NO_3^- in groundwater during both dry and wet seasons within the study area, with most water samples exhibiting concentrations well below the limit values outlined by class III groundwater quality standards (SO_4^{2-} limit value is 250 mg/L; NO_3^- limit value is 20

mg/L). The concentrations of SO_4^{2-} in water samples at sampling points S1, S9, and S45 during the dry season were 558.35, 324.38, and 392.18 mg/L, respectively. The concentration of NO_3^- in water samples at sampling points S1 and S45 was 36.18 and 79 mg/L, respectively. The concentration of SO_4^{2-} in water samples at sampling points S1, S9, and S45 was 417.86, 246.52, and 413.52 mg/L, respectively. The concentration of NO_3^- in water samples at sampling points S1 and S45 was 48.74 and 92.38 mg/L, respectively. The concentration of ions in groundwater samples at these three points is much higher than that at other points, and the concentration exceeds the limit of the class III groundwater quality standard. The groundwater at this point may be polluted by sulfate. Feng et al. observed a significant increase in TH, salinity, Cl^- , and SO_4^{2-} concentrations from 1996 to 2014 in the Hongshan coal mine, indicating that contamination primarily occurred after the closure of the mine.¹⁵ A similar study also revealed that the concentration of SO_4^{2-} in wastewater from numerous wells at a closed coal mine in Shandong Province (closed in 1994) exceeded the drinking water standards.⁶⁴ In addition, the locations of water samples with high ion concentrations in the dry season are consistent with those of water samples with high ion concentrations in the wet season. The increase in rainfall and surface water recharge in the monsoon season results in the SO_4^{2-} concentration of water samples at the same sampling point in the wet season being slightly lower than that in the dry season. It is worth noting that the concentration of NO_3^- in water samples S1 and S45 in the wet season is higher than that in the dry season.

(2) *Spatial Distribution Characteristics of Main Trace Elements.* Figure S9 shows the spatial distribution of Mn and Al elements in groundwater during the dry season and wet season in the study area. The concentration of trace elements in groundwater samples at sampling points distributed along the mainstream of the WMR is generally lower than that of groundwater samples distributed along tributaries and near the mining area. The average content of Mn and Al is lower than that of the class III groundwater quality standard (100 $\mu\text{g/L}$ for Mn and 200 $\mu\text{g/L}$ for Al). The concentrations of Mn and Al at sampling points S1 and S45 during the dry season were 2415.42, 1809.53, 17.58, and 2609.61 $\mu\text{g/L}$, respectively. The concentrations of Mn and Al at S1 and S45 were 1841.84, 1683.55, 24.97, and 2553.29 $\mu\text{g/L}$, respectively. The average Mn concentration of S1 and S45 is 20.29 times and 16.47 times higher than the limit value of groundwater class III water quality standards, respectively. The average Al concentration of S45 is 11.91 times higher than the limit value of the groundwater class III water quality standard, which indicates that the two groundwater samples of S1 and S45 were seriously polluted. Although the manganese ion concentration found in this study is lower than the concentration of Wright' study in the closure of coal mines in Australian manganese (11 909 $\mu\text{g/L}$), it is still a huge hazard to the water environment over time.⁵⁹

3.1.4. *Temporal Variation of Main Ions.* In order to further understand the temporal variation of groundwater chemical components, groundwater samples from S1, S3, S54, and S61 sampling points were selected in the study area. The temporal variation curve diagram of major cations in groundwater was drawn in Figure S10. The peak concentrations of Ca^{2+} , Mg^{2+} , Na^+ , and K^+ in water samples from sampling points S1 and S3 all occurred in December 2021, during the dry season. The peak cation concentration of the S61 sampling site appeared in July 2022, the wet season. The peaks of Ca^{2+} and Na^+ in water

samples from S54 sampling points appeared in July 2022, while the peaks of Mg^{2+} and K^+ appeared in May 2022. The temporal variation of the anion concentration in groundwater is shown in Figure S11. The lowest NO_3^- and Cl^- concentrations in water samples from S1, S3, and S54 sampling points appeared in December 2021, and the peaks appeared in February 2022, July 2022, and April 2022, respectively. Similarly, the SO_4^{2-} concentration at these four sampling points showed a rapid decline trend and reached the lowest value in May 2022, but the peak appeared in December 2021, July 2022, and June 2022, respectively. The irregularity of the temporal changes of cations and ions in groundwater samples at different sampling points may be related to the combined sources of natural contribution and anthropogenic input. Considering that the chemical composition of groundwater in the study area is mainly affected by rock weathering, the difference in the lithology distribution in space may be the main reason for this phenomenon. Second, a large number of cultivated lands is distributed in the study area, and agricultural activities such as fertilization may also have a certain impact on the groundwater's chemical composition.^{18,65}

Figure S12 depicts the temporal evolution of select trace elements in groundwater samples S1, S3, S54, and S61. The concentration values of Li and B elements in the same groundwater sample exhibit similar temporal trends, as illustrated in Figure S12 for S1, S54, and S61. The concentration levels of the Mn and Al elements exhibit similar variations across the time series (S54 and S61). However, notable dissimilarities exist in the temporal variability of trace elements across diverse groundwater samples. For instance, the peak concentrations of lithium (Li) and boron (B) elements in S1 were observed in December 2021 during the dry season, whereas the highest concentrations of Li and B elements in S61 were recorded in July 2022 during the wet season. The highest concentrations of Mn and Al in water sample S54 were observed in December 2021 during the dry season, whereas the peak concentrations of Mn and Al in water sample S61 occurred in April 2022 during the normal season. The primary rock undergoes weathering-induced decomposition, resulting in the precipitation of a fraction of Li from the mineral lattice. Subsequently, Li undergoes migration in an aqueous solution through its combination with halogen elements to generate soluble salts such as LiCl . Therefore, the concentration of Li^+ in groundwater is intricately connected to that present in the surrounding soil. Furthermore, the weathering and dissolution of silicate rock minerals in the study area constitute one of the primary sources of Li found in groundwater. In nature, the boron ion is B^{3-} , possessing weak deformation ability but a strong main polarization ability. It has the capability to form complex ions such as $(\text{BO}_3)^{3-}$ and $(\text{BO}_4)^{5-}$, which coexist in rock-forming minerals. These minerals that form rocks and contain boron release a significant amount of boron ions into groundwater. The concentrations of Mn and Al in groundwater are primarily determined by the hydrogeochemical interactions with soil or rock formations.¹⁹ However, these levels generally remain low enough to not present any significant risks to human health. However, the discharge of untreated industrial and mining wastewater, as well as domestic sewage, can result in soil pollution, while waste dumps contribute to an elevation in the heavy metal concentration in groundwater via runoff.

3.2. *Hydrodynamic Modeling and Water Budget of the WMR Watershed.* 3.2.1. *Calibration and Validation of the Groundwater Flow Model.* (1) *Water Level Fitting Verification.* During the stage of model identification and verification,

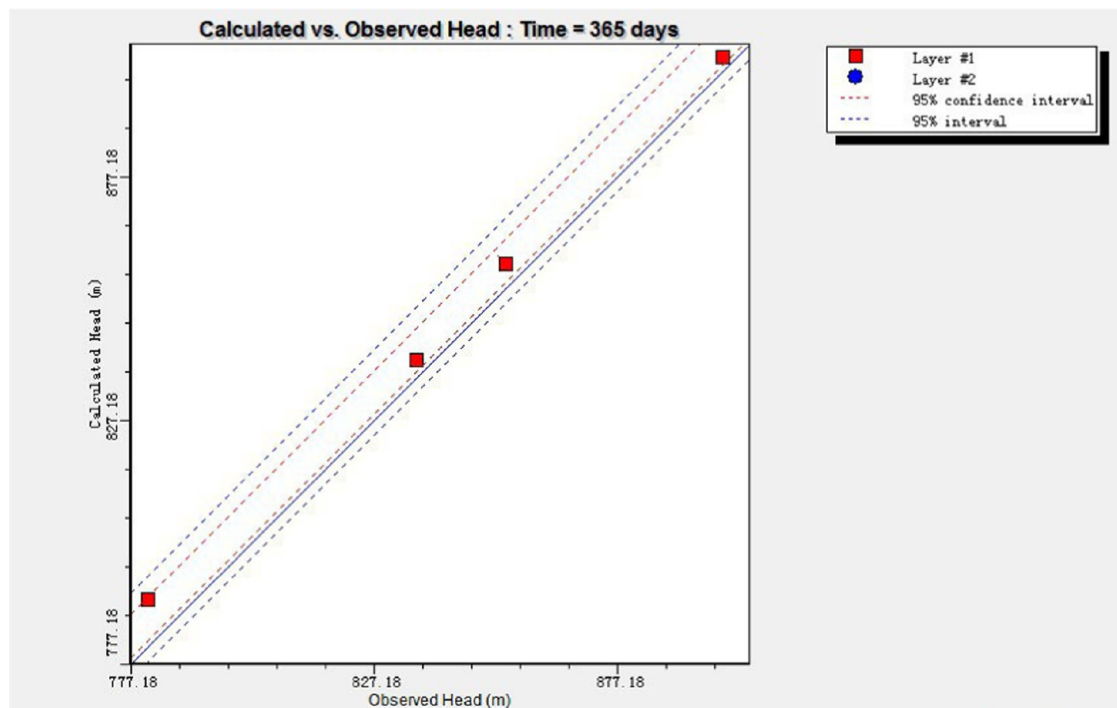


Figure 6. Fitting results of observed and calculated water level values.

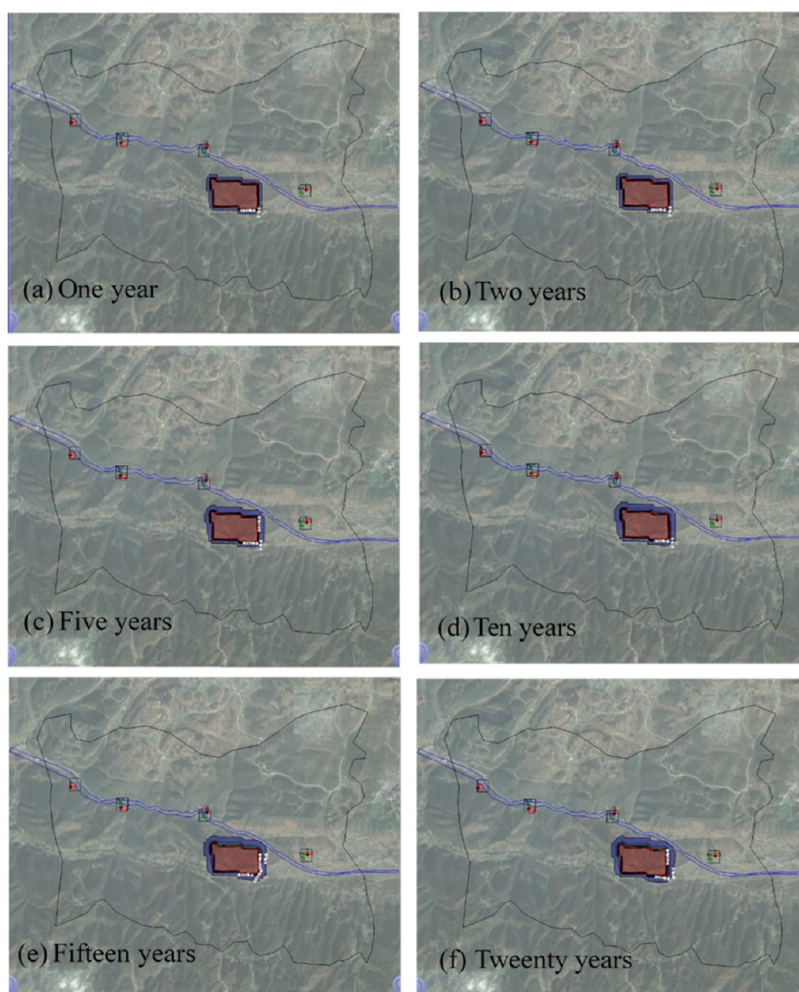


Figure 7. Pollution distribution of Fe in the Longtan Formation.

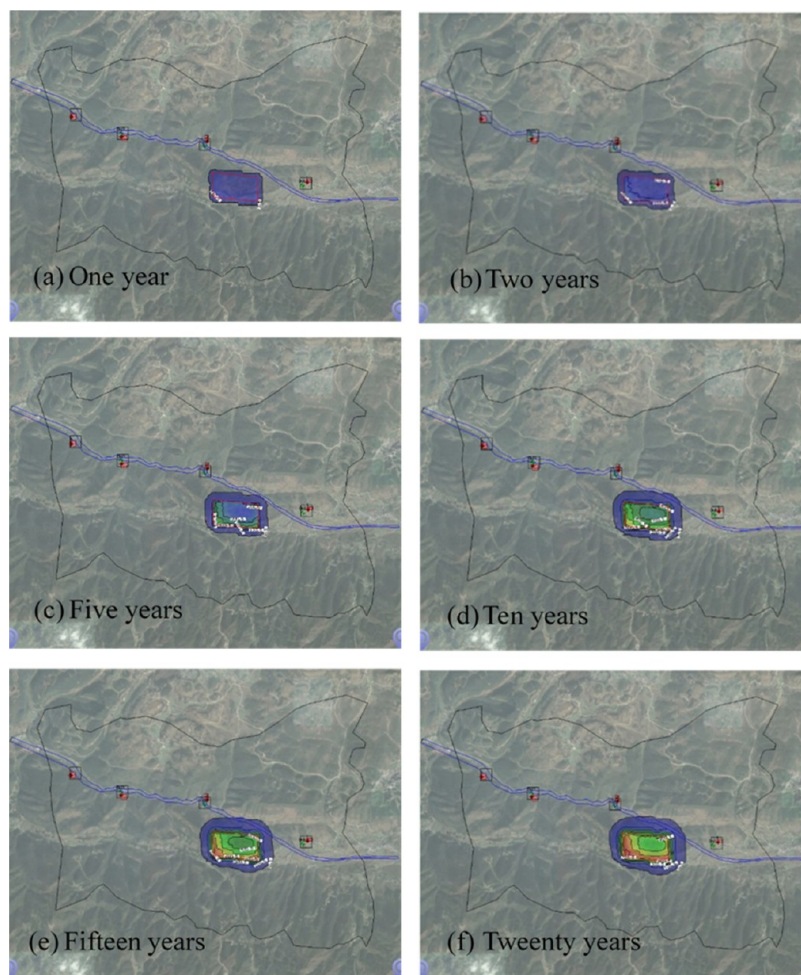


Figure 8. Pollution Distribution of Fe in the Changxing Formation.

the conformity between simulated and actual groundwater levels was evaluated by utilizing borehole water level observation data from 2019 to 2020 in the mining area based on previous data collection and investigation results. With the data of January 2020 as the identification and verification period of the model, it can be seen from Table S7 that the relative error between the measured drilling water level and the simulated calculated water level selected in this study is less than 2%, which basically meets the requirements of simulation accuracy. Additionally, the groundwater level values depicted in Figure 6 exhibit close proximity to their simulated counterparts, indicating an acceptable degree of fit between the two data sets. In summary, the established groundwater flow model has been identified and verified to demonstrate a good simulation effect. This better reflects the groundwater system in the study area and can be utilized for studying and analyzing the migration of groundwater pollutants, as well as managing prevention and control measures.

(2) *Water Balance Analysis.* In order to ensure consistency between the simulated groundwater system and the actual groundwater system, it is necessary to satisfy the water balance conditions while fitting the water level. The verification of the water balance component in the model primarily involves analyzing whether the groundwater recharge rate in the study area satisfies the balance requirement and subsequently assessing the accuracy and reliability of the model. During the simulation period of the model, as illustrated in Table S8, a total recharge of $339.05 \times 10^4 \text{ m}^3$ was observed within the simulated

area, predominantly resulting from rainfall infiltration recharge. The overall excretion amounted to $330.78 \times 10^4 \text{ m}^3$, primarily attributed to evaporation with a minor contribution from lateral outflow. Therefore, according to the amount of recharge and excretion during the simulation period of the model, the calculated equilibrium difference is $59.72 \times 10^4 \text{ m}^3$, which basically belongs to the equilibrium state.

3.2.2. *Simulation and Prediction of Pollutant Transport.* Based on the numerical model of groundwater flow in the closed mine, the MT3D module of Visual MODFLOW software is applied to establish a numerical model for solute transport in the study area's groundwater system, facilitating simulation and prediction of pollutant migration patterns.⁶⁶ According to the aforementioned, in conjunction with a numerical model of groundwater flow, the characteristics of Fe migration within natural groundwater environments by adjusting parameters such as migration direction, range, and concentration changes of Fe pollution were simulated. The polluted layer is located in the coal mining area of Longtan Formation, surrounded by overlying strata of Changxing Formation limestone, middle Yelang Formation limestone, lower Yelang Formation mudstone, and Jialingjiang Formation, as well as underlying strata of Maokou Formation limestone and Qixia Formation limestone.

3.2.3. *Horizontal Interlayer Pollution Process of Groundwater.* (1) *Horizontal Interlayer Pollution in Longtan Formation.* The pollution layer is situated within the Longtan Formation, where coal seams incline at angles ranging from

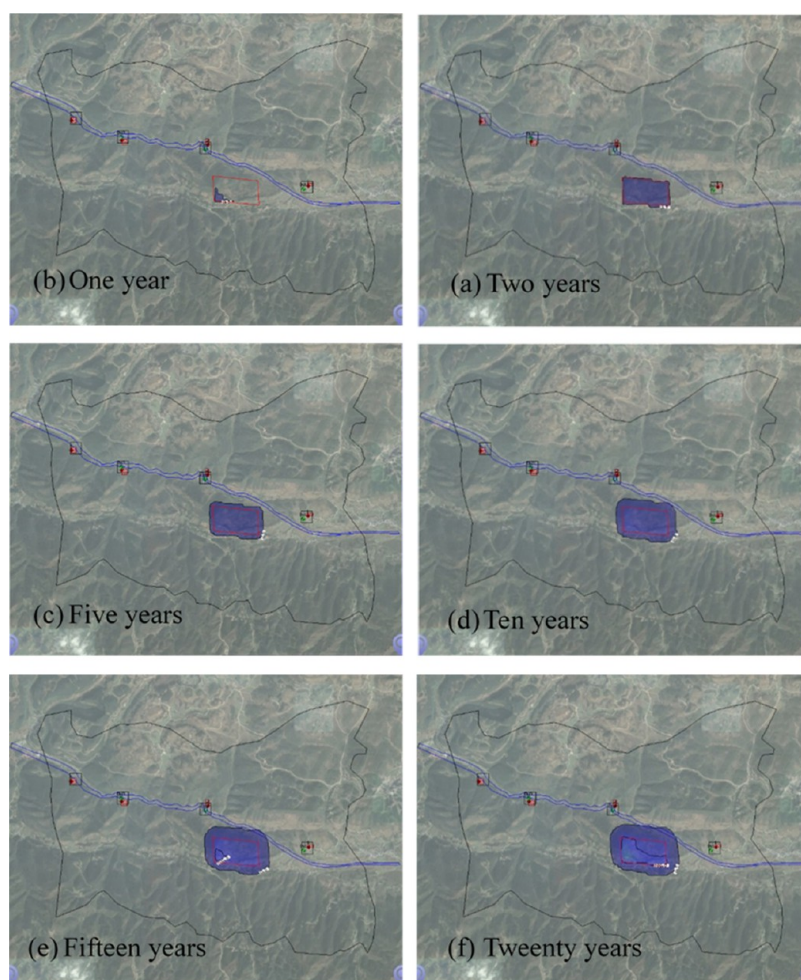


Figure 9. Pollution dispersion diagram of the Yelang group.

approximately 6 to 15°, with an overall inclination of 30°. This formation comprises sandstone, shale, a small amount of limestone, and coal seams. There are seven to 13 layers of coal present, among which three recoverable coal seams exist. Measuring between 80 and 105 m in thickness and exhibiting a zonal distribution pattern, this group displays limited permeability.

The initial concentration of Fe in the adit water postpit closure is approximately 800 mg/L, with a pollution range that spans the entirety of the mining area. The specific spatial positioning and profile morphology are depicted in Figure 7. Numerical simulation software was utilized to model the migration and diffusion of Fe between layers over a period of 1, 2, 5, 10, 15, and 20 years into the future. The layer exhibits low permeability, indicating a relatively impermeable nature. Pollutant diffusion in the horizontal direction is sluggish within this stratum, with a maximum range of 172 m after two decades.

(2) *Horizontal Interlayer Pollution in the Overlying Changxing Formation.* The integration of the Changxing Formation limestone in contact with the polluted layer Longtan Formation is a gray and dark gray giant thick limestone with a thickness of about 50–65 m. Due to the destruction of the Longtan Formation by mining, pollutants were in direct contact with the ground of the Changxing Formation. The bottom erosion surface of a part of the WMR is located in this group, and pollutants enter the WMR through the Changxing Formation. As depicted in Figure 8, the concentration of pollutants in this

group gradually approaches that of WMR at a level of 0.5 mg/L after a period of 5 years.

From the analysis of pollution concentration and range, it is evident that after a period of five years, the total area affected by pollution has expanded to 1.52 km², with an estimated 1.05 km² being attributed to concentrations exceeding 100 mg/L. After 10 years, the cumulative area of pollution has expanded to 2.03 km², with a contamination extent exceeding 100 mg/L covering an area of 1.42 km². After 20 years, the pollution area had expanded to 3.12 km², and the highest concentration of pollutants reached 700 mg/L.

(3) *Horizontal Interlayer Pollution of Middle Yelang Formation Limestone.* The middle limestone of the Yelang Formation constitutes a karstic fissure aquifer composed of marl and argillaceous limestone, with an approximate thickness of 128 m. Through simulation, it can be observed that the pollution layer will overflow and contaminate this stratum within one year (Figure 9). After 10 years, the area of contamination, with pollution concentrations ranging from 0.5 to 100 mg/L, covered a total of 1.44 m². After 15 years, the area with a pollutant concentration exceeding 100 mg/L measured 0.20 m², which increased to 0.75 m² after 20 years.

(4) *Horizontal Interlayer Pollution of Limestone in the Lower Overlying Maokou Formation and Qixia Formation.* The overlying strata of the pollution layer in the Longtan Formation are Maokou Formation and Qixia Formation limestone; the total thickness of the two groups is about 135

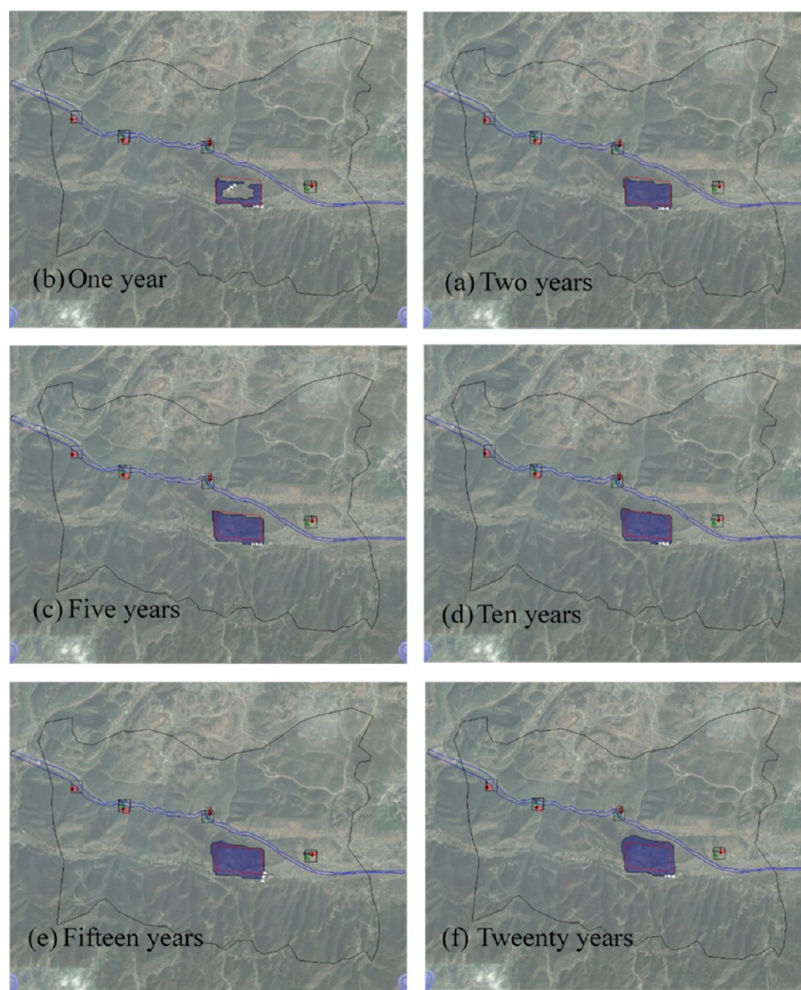


Figure 10. Pollution range map of limestone in the Maokou Formation and Qixia Formation.

m (Figure 10). The pollutants infiltrate the stratum after a year, and their spread expands with time. However, it remains confined within a smaller area compared to that of the overlying Changxing limestone and Yelang limestone.

3.2.4. Vertical Overflow Recharge Pollution Process. To investigate the formation of overflow recharge in the polluted layer of the Longtan Formation, sections A–A' and B–B' were established above the goaf, as illustrated in Figure S13.

The anticipated levels of pollutants in sections A–A' and B–B' of the Longtan Formation subsequent to the cessation of mining activities were illustrated in Figures 11 and 12. After the closure of the mine, the water level within it rose, leading to a rapid spread of pollutants into the surrounding areas. Within one year, these contaminants had infiltrated the aquifer of the overlying Changxing Formation and some have even penetrated into the limestone waters of both Maokou and Qixia Formations below. After 2 years, the pollutants completely entered the lower limestone layer, and the initial concentration was small, basically 0.1–1.5 mg/L. Five years later, the pollutants breached the mudstone barrier in the lower section of the overlying Yelang Formation and infiltrated into the surface water. Subsequently, their concentration gradually escalated until 20 years later when some surface water reached a concentration of 100 mg/L. Due to the obstruction of the mudstone barrier in the lower part of the Yelang Formation, certain pollutants infiltrate into the

Jialingjiang Formation and subsequently migrate horizontally, ultimately recharging WMR and causing its pollution.

According to our prediction, even 20 years after the closure of the coal mine, the pollution resulting from alterations in the earth's water chemistry will persist at a significant level. Belmer et al. found that zinc and nickel concentrations were highest downstream of two closed mines, particularly from the Canyon mine that closed 20 years earlier.⁶⁷ These studies demonstrated that ecologically hazardous water pollution may occur for years after underground coal mines ceased mining.⁶⁴

3.2.5. Pollution Process of WMR. The WMR is successively cut from east to west in the study area, namely, Longtan, Changxing, Yelang, and Jialingjiang formations. The Longtan Formation, Changxing Formation, Yelang Formation, and Jialingjiang Formation are located at a horizontal distance of 150 m and a vertical distance of 350 m from the river in the northeast of the closure area. The WMR watershed is mainly affected by the limestone water of the Changxing Formation and a small amount of Yelang Formation limestone. According to the pollution prediction of Yelang Formation, it is projected that within 5 years, pollutants will infiltrate into the underlying strata of WMR from Changxing Formation. Ten years later, pollutants infiltrated the WMR via the Yelang Formation. As depicted in Figure 13, the peak concentration of pollutants entering the river reached 100 mg/L after two decades. The predicted results show that pollutants can produce cross-rock pollution. Research at the

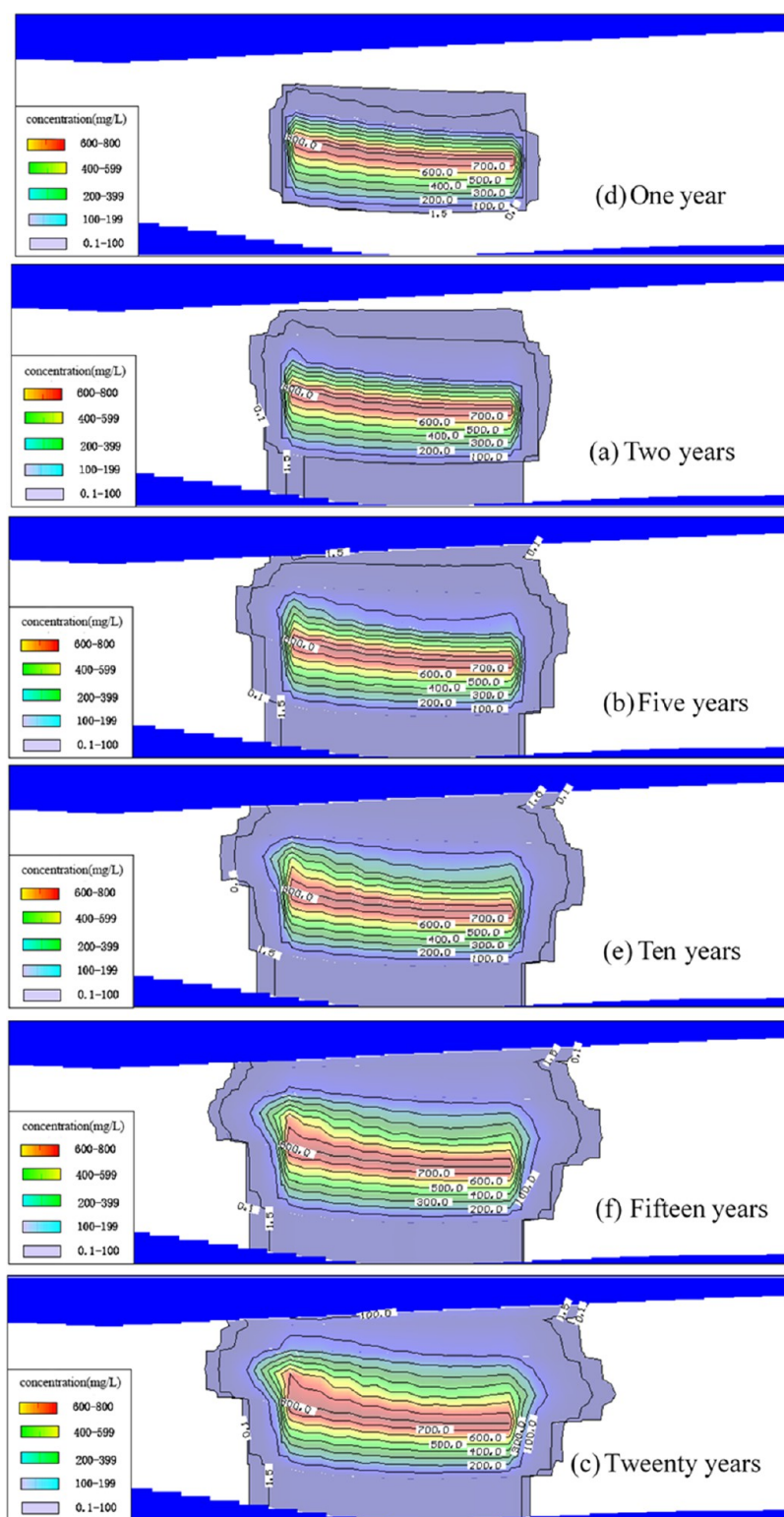


Figure 11. Scope of contaminant pollution in the A–A profile.

Hongshan coal mine in north China confirmed the Ordovician limestone water contamination after closure was owing to cross-strata pollution from mine water, mainly through water conduction fissures, fault structures, and wells with a poor water sealing effect.¹⁵

Through hydrochemical analysis, this study successfully identified and characterized the primary hydrochemical composition within the Wuma River basin, thereby offering

valuable theoretical guidance for future research on coal mine closure. The results obtained from the previous hydrochemical method were further validated through principal component analysis and the factor molecule method. More importantly, the model's prediction enables the definition of hydrological characteristics of pollution in complex underground structures with greater precision and accuracy.

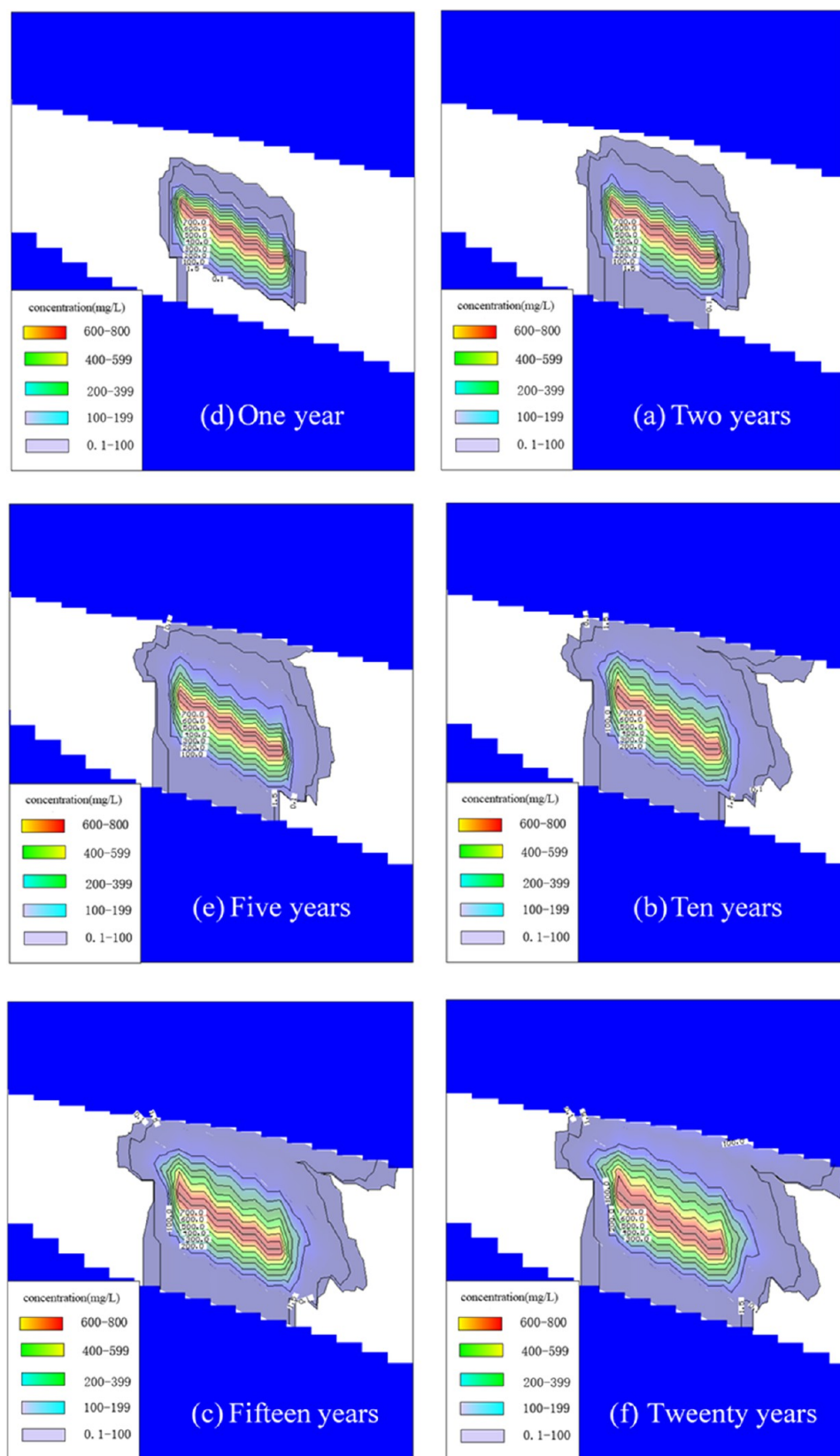


Figure 12. Scope of contaminant pollution in the B–B' profile.

4. CONCLUSIONS

This study demonstrates the effectiveness of a combined approach (geochemical characterization and modeling) on the assessment of groundwater and prediction of pollutants in the

WMR watershed. A geochemical analysis was conducted of the groundwater in WMR. The statistical analysis reveals that the concentrations of the cationic and anionic of groundwater are in the order: $\text{Ca}^{2+} > \text{Mg}^{2+} > \text{Na}^+ > \text{K}^+$, $\text{SO}_4^{2-} > \text{HCO}_3^- > \text{NO}_3^- >$

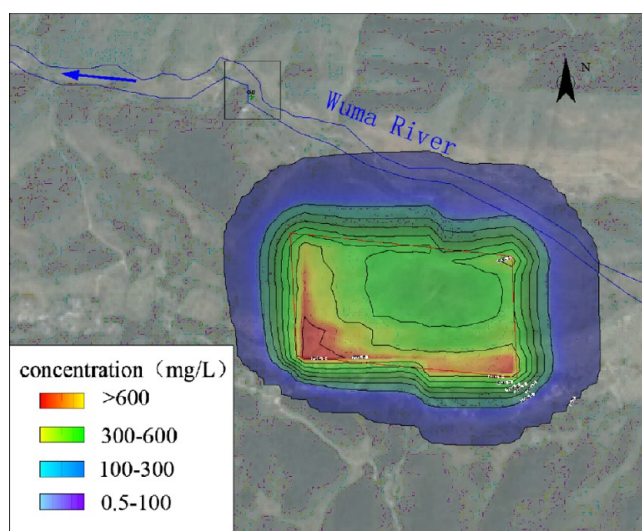


Figure 13. Concentration of pollutants from the Changxing Formation flowing into WMR after 20 years.

Cl^- . The predominant hydrochemical facies are $\text{Ca}^{2+}\text{-Mg}^{2+}\text{-HCO}_3^-$ and $\text{Ca}^{2+}\text{-Mg}^{2+}\text{-SO}_4^{2-}$. Principal correlation analysis was used to gain insight into water–rock interactions taking place in the closure mining regional groundwater. It was demonstrated that the process of the groundwater–rock interaction is characterized by the enrichment of groundwater through the presence of sulfate, calcium, potassium, chloride, and magnesium. The major ion composition in the WMR watershed is a result of mineral weathering and dissolution, which are influenced by ion exchange processes. These two processes are the most significant factors that govern groundwater chemistry. The ion concentration levels at different sampling points are different in both time and space. Subsequently, a hydrogeological Modflow model was calibrated and validated for the mine closure of the WMR watershed, which shows good robustness. Furthermore, the pollution of Fe in different formations was predicted in the future. Over time, various formations generate varying levels of pollution at different rates. The migration direction of pollutants in groundwater mainly migrates along the direction of groundwater flow and diffuses to the direction of vertical flow. Its migration range is consistent with the groundwater flow direction and extends along the larger hydraulic gradient.

■ ASSOCIATED CONTENT

SI Supporting Information

The Supporting Information is available free of charge at <https://pubs.acs.org/doi/10.1021/acsomega.3c05631>.

Location and sampling sites map of the study area (Figure S1); stratigraphic profile of the study area (Figure S2); model scope and boundary diagram (Figure S3); model grid segmentation diagram samples (Figure S4); distribution characteristics of trace elements in groundwater (Figure S5); spatial interpolation of the main pollution factor SO_4^{2-} (Figure S6); spatial distribution characteristics of cations in groundwater (Figure S7); spatial distribution characteristics of anions in groundwater (Figure S8); spatial distribution characteristics of trace elements in groundwater (Figure S9); temporal variations of cation concentrations in groundwater (Figure S10); temporal variations of anionic in groundwater (Figure

S11); temporal variations of trace elements in groundwater (Figure S12); location map of the overflow recharge profile (Figure S13); hydrodynamic parameters of the hydrogeological system of the WMR watershed (Table S1); data processing software and its applications (Table S2); correlation matrix of main ions in groundwater samples during the dry period (Table S3); correlation matrix of major ions in groundwater samples during the wet period (Table S4); load matrix of the maximum rotation factor for groundwater chemical factors' variance in the study area (Table S5); comparative analysis of observed and simulated water level results (Table S6); and groundwater balance table in the simulated area (Table S7) (PDF)

■ AUTHOR INFORMATION

Corresponding Author

Liyang Liang – School of Materials and Environment, Guangxi Minzu university, Nanning 530000, China; Guangxi Chemical Research Institute Limited Company, Nanning 530000, China; Guangxi Colleges and Universities Key Laboratory of Environmental-friendly Materials and New Technology for Carbon Neutralization, Guangxi Key Laboratory of Advanced Structural Materials and Carbon Neutralization, School of Materials and Environment, Guangxi Minzu University, Nanning 530105, China; orcid.org/0009-0005-7973-4764; Email: Liangliyang023@163.com

Authors

Lei Yang – School of Geosciences and Surveying Engineering, China University of Mining and Technology, Beijing 100083, China

Lang Liu – School of Materials and Environment, Guangxi Minzu university, Nanning 530000, China; Guangxi Colleges and Universities Key Laboratory of Environmental-friendly Materials and New Technology for Carbon Neutralization, Guangxi Key Laboratory of Advanced Structural Materials and Carbon Neutralization, School of Materials and Environment, Guangxi Minzu University, Nanning 530105, China

Yuan Liu – Guizhou Environment and Engineering Appraisal Center, Guiyang 550002 Guizhou, China

Guangping Chen – Guizhou ZhongGui Environmental Technology Co., Ltd., Guiyang 550008, China

Complete contact information is available at:

<https://pubs.acs.org/doi/10.1021/acsomega.3c05631>

Notes

The authors declare no competing financial interest.

■ ACKNOWLEDGMENTS

The authors are grateful for the financial support provided by the Project of Guizhou Science and Technology Department (no. 20204Y007), the Open Research Fund of the Guangxi Key Laboratory of Water Engineering Materials and Structures, the Guangxi Institute of Water Resources Research under grant no. GXHRI-WEMS-2022-10, Talent Introduction for Scientific Research in 2021 of Guangxi Minzu University (no. 2021KJQD30), and the Youth Basic Ability Improvement Project in 2023 (no. 302540442).

REFERENCES

- (1) Zhang, H.; Xu, G.; Chen, X.; Mabaire, A.; Zhou, J.; Zhang, Y.; et al. Groundwater Hydrogeochemical Processes and the Connectivity of Multilayer Aquifers in a Coal Mine with Karst Collapse Columns. *Mine Water Environ.* **2020**, *39* (2), 356–368.
- (2) Wang, D.; Wu, J.; Wang, Y.; Ji, Y. Finding High-Quality Groundwater Resources to Reduce the Hydatidosis Incidence in the Shiqu County of Sichuan Province, China: Analysis, Assessment, and Management. *Expo. Health* **2020**, *12* (2), 307–322.
- (3) Chu, X.; Ma, Z.; Wu, D.; Wang, H.; He, J.; Chen, T.; et al. High Fe and Mn groundwater in the Nanchang, Poyang Lake Basin of China: hydrochemical characteristics and genesis mechanisms. *Environ. Monit. Assess.* **2023**, *195* (1), No. 124.
- (4) Houatmia, F.; Azouzi, R.; Charef, A.; Bédir, M. Assessment of groundwater quality for irrigation and drinking purposes and identification of hydrogeochemical mechanisms evolution in North-eastern, Tunisia. *Environ. Earth Sci.* **2016**, *75* (9), No. 746.
- (5) Wang, L.; Dong, Y.; Xu, Z.; Qiao, X. Hydrochemical and isotopic characteristics of groundwater in the northeastern Tengger Desert, northern China. *Hydrogeol. J.* **2017**, *25* (8), 2363–2375.
- (6) Sharma, G. K.; Jena, R. K.; Ray, P.; Yadav, K. K.; Moharana, P. C.; Cabral-Pinto, M. M. S.; Bordoloi, G. Evaluating the geochemistry of groundwater contamination with iron and manganese and probabilistic human health risk assessment in endemic areas of the world's largest River Island, India. *Environ. Toxicol. Pharmacol.* **2021**, *87*, No. 103690.
- (7) Liang, Y.; Gao, X.; Zhao, C.; Tang, C.; Shen, H.; Wang, Z.; Wang, Y. Review: Characterization, evolution, and environmental issues of karst water systems in Northern China. *Hydrogeol. J.* **2018**, *26* (5), 1371–1385.
- (8) Liu, J.; Hao, Y.; Gao, Z.; Wang, M.; Liu, M.; Wang, Z.; Wang, S. Determining the factors controlling the chemical composition of groundwater using multivariate statistics and geochemical methods in the Xiqu coal mine, North China. *Environ. Earth Sci.* **2019**, *78* (12), No. 364.
- (9) Zhu, G.; Wu, X.; Ge, J.; Liu, F.; Zhao, W.; Wu, C. Influence of mining activities on groundwater hydrochemistry and heavy metal migration using a self-organizing map (SOM). *J. Cleaner Prod.* **2020**, *257*, No. 120664.
- (10) Bingxiang, H.; Jiangwei, L.; Nan, L. I.; Xinglong, Z. Framework of the theory and technology for mine closure. *J. China Univ. Min. Technol.* **2017**, *46* (4), 715–729.
- (11) Ayub, A.; Ahmad, S. S. Seasonal Assessment of Groundwater Contamination in Coal Mining Areas of Balochistan. *Sustainability* **2020**, *12* (17), 6889.
- (12) Chen, D.; Feng, Q.; Gong, M. Contamination Characteristics and Source Identification of Groundwater in Xishan Coal Mining Area of Taiyuan Based on Hydrochemistry and Sulfur–Oxygen Isotopes. *Water* **2023**, *15* (6), 1169.
- (13) Song, K.; Wang, F.; Peng, Y.; Liu, J.; Liu, D. Construction of a hydrogeochemical conceptual model and identification of the groundwater pollution contribution rate in a pyrite mining area. *Environ. Pollut.* **2022**, *305*, No. 119327.
- (14) Adamovic, D.; Ishiyama, D.; Kawaraya, H.; Ogawa, Y.; Stevanovic, Z. Geochemical characteristics and estimation of groundwater pollution in catchment areas of Timok and Pek Rivers, Eastern Serbia: Determination of early-stage groundwater pollution in mining areas. *Groundwater Sustainable Dev.* **2022**, *16*, No. 100719.
- (15) Feng, H.; Zhou, J.; Chai, B.; Zhou, A.; Li, J.; Zhu, H.; et al. Groundwater environmental risk assessment of abandoned coal mine in each phase of the mine life cycle: a case study of Hongshan coal mine, North China. *Environ. Sci. Pollut. Res. Int.* **2020**, *27* (33), 42001–42021.
- (16) Liu, P.; Hoth, N.; Drebenstedt, C.; Sun, Y.; Xu, Z. Hydrogeochemical paths of multi-layer groundwater system in coal mining regions — Using multivariate statistics and geochemical modeling approaches. *Sci. Total Environ.* **2017**, *601–602*, 1–14.
- (17) Li, Y.; Hu, F. S.; Xue, Z. Q.; Yu, Y. Q.; Wu, P. Hydrogeochemical and isotopic characteristics of groundwater in the salt chemical industrial base of Guyuan City, northwestern China. *Arabian J. Geosci.* **2015**, *8* (6), 3427–3440.
- (18) Mu, W.; Wu, X.; Wu, C.; Hao, Q.; Deng, R.; Qian, C. Hydrochemical and environmental isotope characteristics of groundwater in the Hongjiannao Lake Basin, Northwestern China. *Environ. Earth Sci.* **2021**, *80* (2), No. 51.
- (19) De Meyer, C. M. C.; Rodríguez, J. M.; Carpio, E. A.; García, P. A.; Stengel, C.; Berg, M. Arsenic, manganese and aluminum contamination in groundwater resources of Western Amazonia (Peru). *Sci. Total Environ.* **2017**, *607–608*, 1437–1450.
- (20) Alkhatib, J.; Engelhardt, I.; Ribbe, L.; Sauter, M. An integrated approach for choosing suitable pumping strategies for a semi-arid region in Jordan using a groundwater model coupled with analytical hierarchy techniques. *Hydrogeol. J.* **2019**, *27* (4), 1143–1157.
- (21) Barclay, J. R.; Briggs, M. A.; Moore, E. M.; Starn, J. J.; Hanson, A. E. H.; Helton, A. M. Where groundwater seeps: Evaluating modeled groundwater discharge patterns with thermal infrared surveys at the river-network scale. *Adv. Water Resour.* **2022**, *160*, No. 104108.
- (22) Hamdi, M.; Zagrarni, M. F.; Djamai, N.; Jerbi, H.; Goita, K.; Tarhouni, J. 3D geological modeling for complex aquifer system conception and groundwater storage assessment: Case of Sisseb El Alem Nadhour Saouaf basin, northeastern Tunisia. *J. Afr. Earth Sci.* **2018**, *143*, 178–186.
- (23) Zhu, R.; Croke, B. F. W.; Jakeman, A. J. Diffuse groundwater recharge estimation confronting hydrological modelling uncertainty. *J. Hydrol.* **2020**, *584*, No. 124642.
- (24) Rödiger, T.; Geyer, S.; Odeh, T.; Siebert, C. Data scarce modelling the impact of present and future groundwater development on Jordan multiaquifer groundwater resources. *Sci. Total Environ.* **2023**, *870*, No. 161729.
- (25) Yousif, M.; Sabet, H. S.; Ghoubachi, S. Y.; Aziz, A. Utilizing the geological data and remote sensing applications for investigation of groundwater occurrences, West El Minia, Western Desert of Egypt. *NRIAG J. Astronomy Geophys.* **2018**, *7* (2), 318–333.
- (26) Jerbi, H.; Hamdi, M.; Snoussi, M.; Ben Abdelmalek, M.; Jnoub, H.; Tarhouni, J. Usefulness of historical measurements of tritium content in groundwater for recharge assessment in semi-arid regions: application to several aquifers in central Tunisia. *Hydrogeol. J.* **2019**, *27* (5), 1645–1660.
- (27) Preziosi, E.; Guyennon, N.; Petrangeli, A. B.; Romano, E.; Di Salvo, C. A Stepwise Modelling Approach to Identifying Structural Features That Control Groundwater Flow in a Folded Carbonate Aquifer System. *Water* **2022**, *14* (16), 2475.
- (28) Ac, A.; Jm, N.; Rw, S.; Ak, M. Groundwater remediation optimization using Solving Constraint Integer Program (SCIP). *Groundwater Sustainable Dev.* **2018**, *7*, 176–184.
- (29) Alexander, A. C.; Ndambuki, J. M. Optimal design of groundwater pollution management systems for a decanting contaminated site: A simulation-optimization approach. *Groundwater Sustainable Dev.* **2021**, *15*, No. 100664.
- (30) Alexander, A. C.; Ndambuki, J. M. Impact of mine closure on groundwater resource: Experience from Westrand Basin-South Africa. *Phys. Chem. Earth. Parts A/B/C* **2023**, *131*, No. 103432.
- (31) Munyengabe, A.; Zvinowanda, C.; Zvimba, J. N.; Ramontja, J. Innovative oxidation and kinetic studies of ferrous ion by sodium ferrate (VI) and simultaneous removal of metals from a synthetic acid mine drainage. *Phys. Chem. Earth. Parts A/B/C* **2021**, *124*, No. 102932.
- (32) Yigit, E.; Yurtsever, A.; Basaran, S. T.; Sahinkaya, E. Optimization of arsenic removal from an acid mine drainage in an anaerobic membrane bioreactor. *Environ. Technol. Innov.* **2020**, *18*, No. 100712.
- (33) Nogueira, E. W.; Gouvêa De Godoi, L. A.; Marques Yabuki, L. N.; Brucha, G.; Zamariolli Damjanovic, M. H. R. Sulfate and metal removal from acid mine drainage using sugarcane vinasse as electron donor: Performance and microbial community of the down-flow structured-bed bioreactor. *Bioresour. Technol.* **2021**, *330*, No. 124968.
- (34) Wang, W.; Qiang, Y.; Wang, Y.; Sun, Q.; Zhang, M. Impacts of Yuyang Coal Mine on Groundwater Quality in Hongshixia Water Source, Northwest China: A Physicochemical and Modeling Research. *Expo. Health* **2016**, *8* (3), 431–442.

- (35) Mal, U.; Adhikari, K. Groundwater quality and hydrological stress induced by Lower Gondwana open cast coal mine. *J. Earth Syst. Sci.* **2021**, *130* (1), No. 32, DOI: 10.1007/s12040-020-01486-x.
- (36) Adhikari, K.; Mal, U. Evaluation of contamination of manganese in groundwater from overburden dumps of Lower Gondwana coal mines. *Environ. Earth Sci.* **2021**, *80* (1), No. 23, DOI: 10.1007/s12665-020-09293-9.
- (37) Kim, S.-M.; Choi, Y. SIMPL: A Simplified Model-Based Program for the Analysis and Visualization of Groundwater Rebound in Abandoned Mines to Prevent Contamination of Water and Soils by Acid Mine Drainage. *Int. J. Environ. Res. Public Health* **2018**, *15* (5), 951.
- (38) Bozan, C.; Wallis, I.; Cook, P. G.; Dogramaci, S. Groundwater-level recovery following closure of open-pit mines. *Hydrogeol. J.* **2022**, *30* (6), 1819–1832.
- (39) Spanidis, P.-M.; Roumpos, C.; Pavloudakis, F. Evaluation of Strategies for the Sustainable Transformation of Surface Coal Mines Using a Combined SWOT–AHP Methodology. *Sustainability* **2023**, *15* (10), 7785.
- (40) Salmani, H.; Javadi, S.; Eini, M. R.; Golmohammadi, G. Compilation simulation of surface water and groundwater resources using the SWAT-MODFLOW model for a karstic basin in Iran. *Hydrogeol. J.* **2023**, *31* (3), 571–587.
- (41) Tarasenko, I.; Kholodov, A.; Zin’Kov, A.; Chekryzhov, I. Chemical composition of groundwater in abandoned coal mines: Evidence of hydrogeochemical evolution. *Appl. Geochem.* **2022**, *137*, No. 105210.
- (42) Jiang, B.-b.; Ji, K.; Xu, D.; Cao, Z.; Wen, S.; Song, K.; Ma, L. Effects of Coal Gangue on the Hydrochemical Components under Different Types of Site Karst Water in Closed Mines. *Water* **2022**, *14* (19), 3110.
- (43) Zhao, X.; Wang, D.; Xu, H.; Ding, Z.; Shi, Y.; Lu, Z.; Cheng, Z. Groundwater pollution risk assessment based on groundwater vulnerability and pollution load on an isolated island. *Chemosphere* **2022**, *289*, No. 133134.
- (44) Ware, H. H.; Mengistu, T. D.; Yifru, B. A.; Chang, S. W.; Chung, I. Assessment of Spatiotemporal Groundwater Recharge Distribution Using SWAT-MODFLOW Model and Transient Water Table Fluctuation Method. *Water* **2023**, *15* (11), 2112.
- (45) Malekzadeh, M.; Kardar, S.; Shabanlou, S. Simulation of groundwater level using MODFLOW, extreme learning machine and Wavelet-Extreme Learning Machine models. *Groundwater Sustainable Dev.* **2019**, *9*, No. 100279.
- (46) Patil, N. S.; Chetan, N. L. Groundwater modeling of Hiranyakeshi watershed of Ghataprabha sub-basin. *J. Geol. Soc. India* **2017**, *90* (3), 357–361.
- (47) Liu, Q.; Hanati, G.; Danierhan, S.; Zhang, Y.; Zhang, Z. Simulation of Groundwater Level in Ephemeral Streams with an Improved Groundwater Hydraulics Model. *Ground Water* **2019**, *57* (6), 969–979.
- (48) Harbaugh, B. A. W.; Banta, E. R.; Hill, M. C.; McDonald, M. G. Modflow-2000, The U.S. Geological Survey Modular Ground-Water Model User Guide To Modularization Concepts And The Ground-Water Flow Process. 2000.
- (49) Rajaeian, S.; Ketabchi, H.; Ebadi, T. Investigation on quantitative and qualitative changes of groundwater resources using MODFLOW and MT3DMS: a case study of Hashtgerd aquifer, Iran. *Environ. Dev. Sustainability* **2023**, DOI: 10.1007/s10668-022-02904-4.
- (50) Chai, Y.; Xiao, C.; Li, M.; Liang, X. Hydrogeochemical Characteristics and Groundwater Quality Evaluation Based on Multivariate Statistical Analysis. *Water* **2020**, *12* (10), 2792.
- (51) Ramachandran, M.; Schwabe, K. A.; Ying, S. C. Shallow Groundwater Manganese Merits Deeper Consideration. *Environ. Sci. Technol.* **2021**, *55* (6), 3465–3466.
- (52) Wang, M.; Gui, H.; Hu, R.; Zhao, H.; Li, J.; Yu, H.; Fang, H. Hydrogeochemical Characteristics and Water Quality Evaluation of Carboniferous Taiyuan Formation Limestone Water in Sulin Mining Area in Northern Anhui, China. *Int. J. Environ. Res. Public Health* **2019**, *16* (14), 2512.
- (53) Capuano, R. M.; Jones, C. R. Cation Exchange in Groundwater-Chemical Evolution and Prediction of Paleo-Groundwater Flow: A Natural-System Study. *Water Resour. Res.* **2020**, *56* (8), No. e2019WR026318.
- (54) Gupta, S.; Nayek, S.; Chakraborty, D. Hydrochemical evaluation of Rangit river, Sikkim, India: using Water Quality Index and multivariate statistics. *Environ. Earth Sci.* **2016**, *75* (7), No. 567.
- (55) Wali, S. U.; Alias, N.; Harun, S. B. Reevaluating the hydrochemistry of groundwater in basement complex aquifers of Kaduna Basin, NW Nigeria using multivariate statistical analysis. *Environ. Earth Sci.* **2021**, *80* (5), No. 208.
- (56) Kumar, P.; Bansod, B. K. S.; Debnath, S. K.; Thakur, P. K.; Ghanshyam, C. Index-based groundwater vulnerability mapping models using hydrogeological settings: A critical evaluation. *Environ. Impact Assess. Rev.* **2015**, *51*, 38–49.
- (57) Machiwal, D.; Jha, M. K. Identifying sources of groundwater contamination in a hard-rock aquifer system using multivariate statistical analyses and GIS-based geostatistical modeling techniques. *J. Hydrol.: Reg. Stud.* **2015**, *4*, 80–110.
- (58) Hamdi, M.; Zagrarni, M. F.; Jerbi, H.; Tarhouni, J. Hydrogeochemical and isotopic investigation and water quality assessment of groundwater in the Sisseb El Alem Nadhour Saouaf aquifer (SANS), northeastern Tunisia. *J. Afr. Earth Sci.* **2018**, *141*, 148–163.
- (59) Wright, I. A.; Paciuszkiewicz, K.; Belmer, N. Increased Water Pollution After Closure of Australia’s Longest Operating Underground Coal Mine: a 13-Month Study of Mine Drainage, Water Chemistry and River Ecology. *Water, Air, Soil Pollut.* **2018**, *229* (3), No. 55, DOI: 10.1007/s11270-018-3718-0.
- (60) Hamdi, M.; Goïta, K.; Karaoui, F.; Zagrarni, M. F. Hydrodynamic groundwater modeling and hydrochemical conceptualization of the mining area of Moulares Redeyef (southwestern of Tunisia): New local insights. *Phys. Chem. Earth. Parts A/B/C* **2021**, *121*, No. 102974.
- (61) Zhang, H.; Xu, G.; Zhan, H.; Chen, X.; Liu, M.; Wang, M. Identification of hydrogeochemical processes and transport paths of a multi-aquifer system in closed mining regions. *J. Hydrol.* **2020**, *589*, No. 125344.
- (62) Lu, P.; Zhang, D.; Chai, Y.; Yu, C.; Wang, X.; Tang, Y.; et al. Regulatory-sequence mechanical biosensor: A versatile platform for investigation of G-quadruplex/label-free protein interactions and tunable protein detection. *Anal. Chim. Acta* **2019**, *1045*, 1–9.
- (63) Qian, J.; Peng, Y.; Zhao, W.; Ma, L.; He, X.; Lu, Y. Hydrochemical processes and evolution of karst groundwater in the northeastern Huaibei Plain, China. *Hydrogeol. J.* **2018**, *26* (5), 1721–1729.
- (64) Zhou, J.; Zhang, Q.; Kang, F.; Zhang, Y.; Yuan, L.; Wei, D.; Lin, S. Using multi-isotopes (³⁴S, ¹⁸O, ²H) to track local contamination of the groundwater from Hongshan-Zhaili abandoned coal mine, Zibo city, Shandong province. *Int. Biodeterior. Biodegrad.* **2018**, *128*, 48–55.
- (65) An, Y.; Lu, W. Hydrogeochemical processes identification and groundwater pollution causes analysis in the northern Ordos Cretaceous Basin, China. *Environ. Geochem. Health* **2018**, *40* (4), 1209–1219.
- (66) Grodzka-Łukaszewska, M.; Nawalany, M.; Zijl, W. A Velocity-Oriented Approach for Modflow. *Transp. Porous Media* **2017**, *119* (2), 373–390.
- (67) Belmer, N.; Wright, I. A. The regulation and impact of eight Australian coal mine waste water discharges on downstream river water quality: a regional comparison of active versus closed mines. *Water Environ. J.* **2020**, *34* (3), 350–363.